Large-scale patterning of π-conjugated materials by meniscus guided coating methods

Mélissa Richard, Abdulelah Al-Ajaji, Shiwei Ren, Antonino Foti, Jacqueline Tran, Michel Frigoli, Boris Gusarov, Yvan Bonnassieux, Enric Garcia Caurel, Pavel Bulkin, et al.

To cite this version:

Mélissa Richard, Abdulelah Al-Ajaji, Shiwei Ren, Antonino Foti, Jacqueline Tran, et al.. Large-scale patterning of π-conjugated materials by meniscus guided coating methods. Advances in Colloid and Interface Science, 2020, 275, pp.102080. 10.1016/j.cis.2019.102080 . hal-02391706

HAL Id: hal-02391706
https://hal.science/hal-02391706v1

Submitted on 4 Jan 2021

Large-scale patterning of π-conjugated materials by meniscus guided coating methods

Mélissa Richard[1], Abdulelah AL-AJAJI[1], Shiwei Ren[1], Antonino Foti[1], Jacqueline Tran[1], Michel Frigoli[2], Boris Gusarov[1], Yvan Bonnassieux[1], Enric Garcia Caurel[1], Pavel Bulkin[1], Razvigor Ossikovski[1], Abderrahim Yassar[1]

1) LPICM, CNRS, Ecole Polytechnique, Institut Polytechnique de Paris, route de Saclay, 91128 Palaiseau, France.

2) UMR CNRS 8180, UVSQ, Institut Lavoisier de Versailles, Université Paris-Saclay, 45 avenue des Etats-Unis, 78035 Versailles Cedex, France.

Keywords: conjugated polymer, solution printing, meniscus guided coating, doctor blade, organic semiconductors, organic field effect transitor, P3HT, conjugated block copolymer morphology, polymer crystallization

ABSTRACT

Printed organic electronics has attracted considerable interest in recent years as it enables the fabrication of large-scale, low-cost electronic devices, and thus offers significant possibilities in terms of developing new applications in various fields. Easy processing is a prerequisite for the development of low-cost, flexible and printed plastics electronics. Among processing techniques, meniscus guided coating methods are considered simple, efficient, and low-cost methods to fabricate electronic devices in industry. One of the major challenges is the control of thin film morphology, molecular orientations and directional alignment of polymer films during coating processes. Herein, the recent progress of emerging field of meniscus guided

printing organic semiconductor materials is discussed. The first part of this report briefly summarizes recent advances in meniscus guided coating techniques. The second part discusses periodic deposits and patterned deposition at moving contact lines, where the mass-transport influences film morphology due to convection at the triple contact line. The last section summarizes our strategy to fabricate large-scale patterning of π-conjugated polymers using meniscus guided method.

I) Introduction

Self-assembly offers a powerful strategy to produce highly ordered and structured materials. In the absence of external influence, self-assembly is driven by energy minimization to form components ranging in size from Angstroms to centimeters[1]. Because of its operability, cost-effectiveness, and wide applicability the evaporative induced self-assembly (EISA) method is one of the most essential synthetic methods and is widely investigated in the fabrication of various functional mesoscopic materials [2, 3]. However, irregular patterns and structures are often observed due to lack of control over the evaporative flux of the solvent and the associated flow within the droplet. To overcome this, controlled EISA concept was introduced and has been recognized as a simple and efficient non-lithography approach for producing a variety of patterns with high regularity of polymers, nanocrystals, carbon nanotubes, etc [2, 4]. Among various EISA techniques, meniscus guided coating (MGC) techniques such as zone casting [5], dip coating [6], solution shearing [7, 8], etc. are attractive methods providing one with simple and economical approach to assembly functional materials with structural hierarchy across a wide range of length scales. MGC method was first developed during the 1940's as a method of forming thin sheets of piezoelectric materials and capacitors and is now one of the widely used techniques for producing thin films on large area surfaces and an accepted precision coating method [9]. In theses methods, the process of film formation relies on applying a unidirectional shear force to the solution that passes through a small gap between the blade and the substrate and produces a controlled thickness. Capillarity forces are the major driving forces for film formation in this process. Thus, solvent evaporation from meniscus induces convective flows which transport solutes to the solvent-substrate contact line. This yields a solute supersaturated phase containing continually aggregated solutes, promoting the thin film formation.

In the last decades, printed electronics has witnessed immense research efforts, technological growth and increased commercial interests because of potentials to produce lightweight, thin, large-scale, low-cost electronic devices and systems, using high-throughput printing technology [10]. The combination of printing technologies with other novel features such as flexibility and stretchability result in new electronics/optics applications in fields such as logic circuits, displays, solar cells, radio-frequency identification tags, sensors etc. The key advantages of printing processes are their ability to offer large-area and high-throughput production capabilities. Recently, solution-processable π-conjugated organic semiconductor (OSC) materials are being highlighted for their potential application in printed organic electronics and many other technological applications such as low-cost, lightweight and flexible optoelectronic devices. Compared to inorganic semiconductors, organic ones have attracted significant attention because of their full compatibility with various printing techniques, which guarantee high-throughput manufacturing by cost-effective continuous printing methods on various desirable substrates. One of the major challenges in this field is the control of thin film morphology, molecular orientations and directional alignment of polymer films during coating processes, which critically influence device performance. In fact, in the solid state the mesoscopic organization of π-conjugated materials is the most important parameter determining their opto-electronic properties and performance in devices. These materials have a tendency to self-assembly. Thus, their cooperative self-assembly provides a facile approach for the rational design and fabrication of functional nanostructured materials across multiple length scales. For instance, the self-assembly of block copolymers (BCPs) in solution as well as in thin films is well-known example of such self-assembly and offers an important and well-developed method for the fabrication of various types of well-ordered nanostructures such as lamellae, cylinders and spheres on a variety of substrates [11]. Printing methods constitute a category of solution-phase deposition techniques; and can be classified into four categories: drop casting, spin coating, meniscus-guided and printing [12]. MGC methods are characterized by the unidirectional passage of a liquid meniscus over a target substrate, doctor blade, shearing solution, implementations of Meyers'rod, hollow-pen, and dip coating are examples of processing where the solution meniscus is crucial for the film deposition. All these techniques are attractive for industrial deployment because they are amenable to high-throughput, continuous deposition, and can also be implemented in roll-to-roll setups. We restrict the discussion here to the MGC methods to deposit OSC crystallites in a unidirectional direction [19].

In MGC method the coating speed is one of most critical parameters that largely determines the film thickness, film crystallinity and morphology. Hence, the solution is deposited on the substrate and forms a standing meniscus between the substrate and the blade, as shown in Figure 1. During the evaporation of the solvent, the meniscus moves with the movement of the top blade. Once the solution attains supersaturation, the solute forms a wet thin film. The wet film thickness can be controlled by adjusting the processing parameters such as the solution concentration, the blade gap, the blade coating speed and the coating temperature, etc.

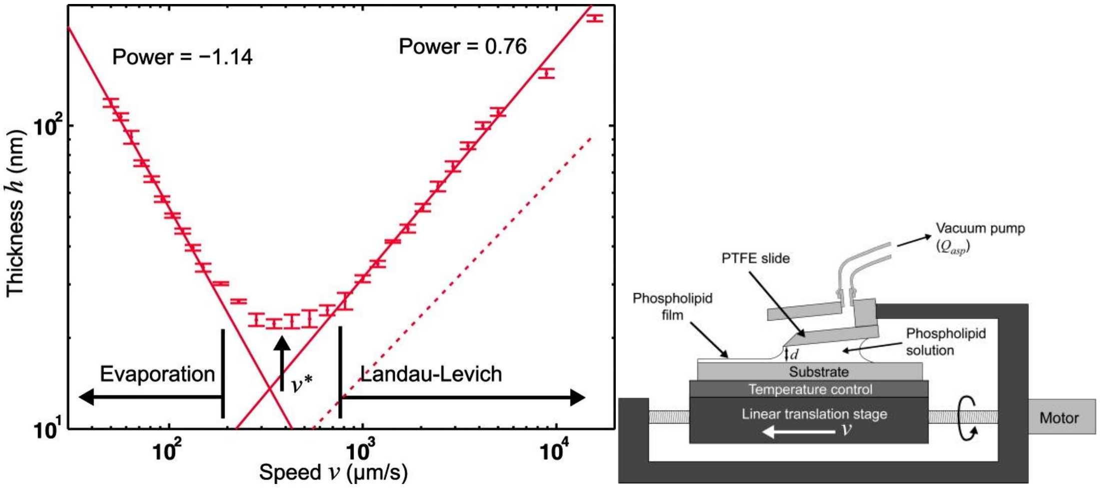

Figure 1. Measured film thickness *h* as a function of deposition speed *v*. Two regimes are identified as a function of *v*: evaporation and Landau−Levich. The solid lines are exponential fits. The dashed line corresponds to the theoritical prediction. Right, experimental setup for film deposition, *v*, *d*, and Q_{asp} are the receding speed, the meniscus height, and the aspiration flow rate, respectively. Reproduced with permission [13].

In these methods, two regimes have been identified depending on the coating speed [13]. At low coating speeds, evaporative regime, where the flow is dominated by evaporation-driven capillary flow resembling the coffee-ring effect. The evaporation induces solute supersaturation at the meniscus, resulting in a dry film. At high speeds, a liquid film is drawn out of the reservoir and dries later on. This regime is often referred to the Landau-Levich regime where the viscous force dominates the convective flow. Thus, the amount of solvent dragged out by the viscous force is larger than the amount of solvent evaporated. The thickness of the liquid film varies by $v^{2/3}$, where v is the coating speed, and can be described by the associated drag-out problem of uniform solvent evaporation. At low coating speeds, the evaporative regime, the deposited film thickness empirically varies as $v^{-1.1}$. In this regime, stick-slip phenomenon is often observed, resulting to formation of regular line patterns of the solute perpendicular to the casting direction. The stick-slip motion of the contact line is a consequence of the competition between pinning and depinning forces. In fact, during the coating process the contact line is not kept pinned, resulting in a stick-slip motion, repeated pinning and depinning. The solutes transport to the edge during pinning of the triple contact line, i.e. stick, thus forming a deposit. Then, the triple contact line jumps, (i.e. slip) to a new position and a deposit is then formed. These pinning and depinning events alternate as solvent evaporates and, ultimately, lead to the formation of periodic deposit, which is governed by a competition between the capillary force and the pinning force. The width, shape and periodicity of the patterns can be manipulated by varying the OSC concentration, speed and surface energy of the substrate. While much work has been focused on high coating speeds, little attention has been paid to the low coating speeds. This is because stick-slip behaviour resulting in a stripe-patterned film, which is not desirable in applicaltions requiring uniform films. The stick–slip phenomenon has been observed for different systems such as small molecules, colloidal suspensions, polymer solutions and sol-gel solutions [14, 15].

This review highlights the recent progress in the emerging field of meniscus-guided deposition of OSC materials, with particular emphasis on materials and physical chemistry of surface thin films that have the potential to achieve improved electrical performance devices. Although several excellent reviews have already examined the field from a printing point of view, addressing critical issues in printing methods for organic electronics [16], organic field-effect transistors (OFETs) materials developed for unidirectional coating methods [17], the confinement effect, fluid flows, and interfacial assembly and the role they play in directing assembly [18], uniaxial backbone alignment of polymers in thin films, with strong transport anisotropy along the alignment direction, with focus an the processing–structure–property relationships [19], flow-directed small molecule crystallization [20]. By contrast, the present review examines advances in the evaporative deposition regime, where mass-transport influences film morphology due to convection at the triple contact line. In section 1, we briefly summarize the recent advances in meniscus guided coating techniques. Then in section 2, we discuss periodic deposits and patterned deposition at moving contact lines. In the last section, we summarize our strategy to fabricate large-scale patterning of π-conjugated polymers by doctor blade coating (DBC) method. We believe this review article can be beneficial for organic electronics community by reporting 1) recent trends in the MGC methods, 2) critical issues in film depotion in the evaporative regime, and 3) advantages of MGC methods and their potential use in large area patterning of π-conjugated materials using cost effective approaches.

II) Recent advances in meniscus guided coating techniques

Because the topic was recently reviewed, we will focus on the most significant results obtained since then, [16], [17], [18], [19], [20]. MGC methods continue to attract considerable attention from the organic electronics community, because their directional coating systems induce large and uniaxial growth of crystals along the coating direction, which is desirable for high performance devices. Besides they are cost-effective methods, which could minimize wastage of materials; and finally they are compatible with large-area manufacturing. In 2017, Chan *et al.* developed a dual solution-shearing method, which successfully generates continuous and highly crystallized semiconductor monolayers with single-crystalline domains in centimeter scale [21]. A solution of 2,9 didecyldinaphtho[2,3-b:2′,3′-f]thieno[3,2-b]thiophene (C10-DNTT) was sheared on phenyltrichlorosilane treated Si/SiO_2 substrate at elevated temperature and the concentration was higher than the solubility limit at this temperature, forming multilayer crystals with different orientations. Then a second-round solution-shearing was carried out with the same concentration at slightly higher temperature. In this way, the second layer and upper layers were dissolved in the second round shearing because of the weaker adhesion between the C10-DNTT molecules than that between the C10-DNTT and the substrate, resulting in high- quality monolayer 2D-crystals. The OFET devices based on monolayer crystals of C10-DNTT show an appreciable carrier mobility of up to 10.4 $cm^2 V^{-1} s^{-1}$, which is the highest among the reported values of solution-processed monolayer devices, as shown by the atomic force microscopy (AFM) image, Figure 2. The growth of crystallized semiconductor monolayer includes process of dissolving and recrystallization. The OFET devices based on the monolayer crystals were used to sense the NH_3. Outstanding sensing performance to NH_3 with a limit of detection as low as 10 ppb was obtained.

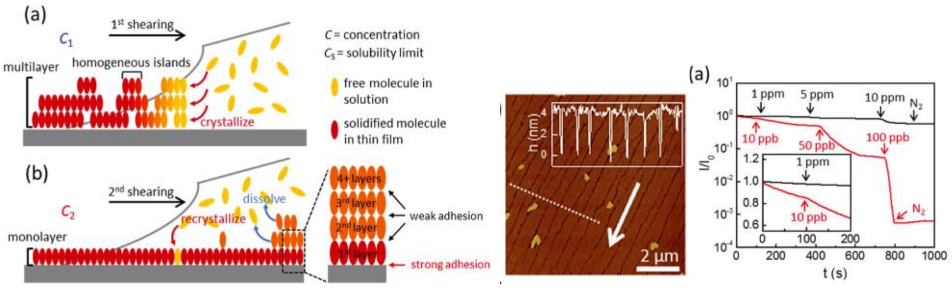

Figure 2. Left, a,b) Schematic drawing of the process of dissolving and recrystallization dual solution-shearing process. Right, AFM image of semiconductor monolayers. White arrow denotes shear direction. Inset: Height profile along white dotted line. Drain–source current response of monolayer- (red) and multilayer-based (black) OFET sensors upon exposure to different concentrations of NH_3. Reproduced with permission [21].

Organic semiconductor single crystals (OSSCs) are now widely recognized as an important tool for making flexible and large area electronics with the compatibility of solution deposition and low coast processing, which leads to low-cost mass manufacturing with a high throughput [22]. Among the various organic electronic devices that can be realized based on OSSCs, the OFET occupies a predominant role. Different methods have been used so far to grow large scale single crystal of OSCs using solution-coating processes, such as drop casting [23], dip coating [24], etc. Among these techniques, a meniscus-driven solution-processed method is promising for the fabrication and scaling-up of uniform OSSCs.

Our pioneer work on solution processable of dibenzo[d,d]thieno[3,2-b;4,5-b’] dithiophene (DBTDT), as an example, focused on the prepation of large area single crystal films of DBTDT for OFET applications using zone-casting technique [25]. The zone-casted layers of DBTDT were successfully applied in a fabrication of OFETs with a Parylene-C, as the gate dielectric. The best parameters are exhibited by the devices with the bottom-gate, top contact configuration with a charge carrier mobility up to 0.02 cm^2 V^{-1} s^{-1}. The performance of these OFETs remains unchanged after one month storage in air. The molecular arrangement of DBTDT zone casted films is similar to single crystal, indicating that the molecules are oriented with their long axis perpendicular to the substrate, Figure 3. The main peak corresponds to d spacing of 1.53 nm, wich is close to DBTDT molecule length, 1.26 nm. The polarized OM images of the zone casted layers of DBTDT on glass substrates confirm the homogenous molecular alignment of the DBTDT molecules on a large area (more than 20 cm^2). Moreover, the material birefringence was observed when the polycrystalline structure was observed between crossed polarizer and analyzer. The AFM images obtained for the layer scratched with needle allows to measure the height difference between the layer and the glass. Thickness of the DBTDT zone cast layer determined in such a way amounted to about 50 nm, which is similar to the thickness of the single crystals. All of these, X-ray investigations, AFM, and polarized optical microscopy (OM) characterizations, are indicative of the formation of large area single crystal films of DBTDT.

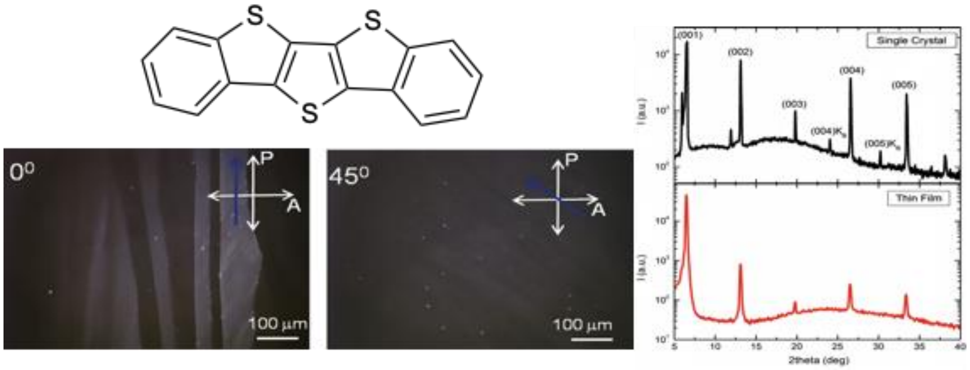

Figure 3. Left, the chemical structure of DBTDT (top). POM images of DBTDT zone casted film (bottom). Blue arrow indicates the casting direction, white arrows show orientations of polarisation planes of polariser and analyser. Right, XRD spectra of single crystal (top) and thin film (bottom). Reproduced with permission [25].

Takeya and co-workers developed selective deposition of monolayer, bilayer, and trilayer molecular OSSC with wafer-scale coverage by optimization of the meniscus-driven crystal growth technique [26]. The OFETs showed the best performance with a mobility that reaches up to 13 cm^2 V^{-1} s$^{-1.}$ These state-of-the-art OFETs allowed high-frequency operation with a channel length of 3 μm and response at a frequency of 20 MHz with an applied voltage of −10 V. In their crystal growth technique, solvent evaporation occurs at the edge of the meniscus region of a droplet retained at a shearing blade, which promotes crystallization from a supersaturated zone of the solution. The solute precipitation rate is critically influenced by the amount of solvent evaporation; substrate temperature, shearing rate of the substrate, and the solution concentration are adjusted to control the number of layers from monolayer to multilayer while achieving large-area coverage. The formation of OSSC films was confirmed by cross-polarized OM and scanning electron microscopy (SEM) observations, Figure 4.

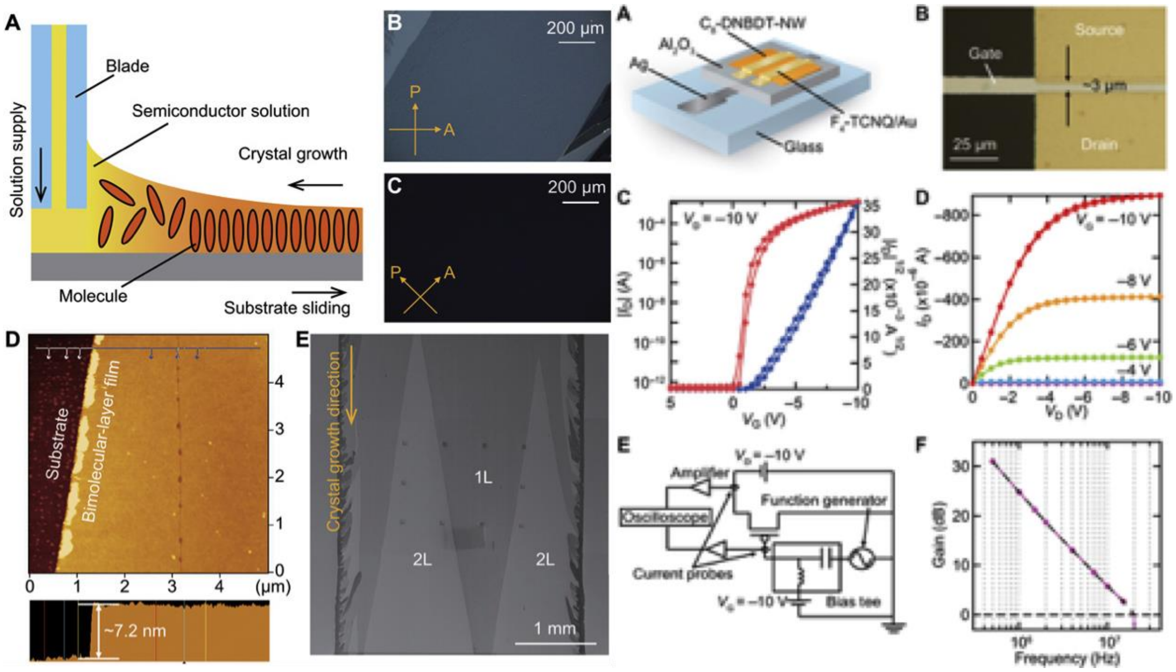

Figure 4. Left, characteristics of ultrathin OSSC films. (A) Schematic image of the continuous OSSC method. (B and C) Cross-polarized OM images of the fabricated ultrathin OSSC. (D) AFM image and cross-sectional profile of the 2L OSSC. (E) Combined SEM image of ultrathin 1L and 2L OSSC films. Right, short-channel 2L-OFET for cutoff frequency measurement. (A) Schematic image of the fabricated 2L-OFET. (B) Micrograph of the 2L-OFET with a channel length of 3 μm. (C) Transfer and (D) output

properties of the fabricated 2L-OFET with $L/W = 3/750$ μm. (E) Schematic diagram of the setup for the cutoff frequency measurement. (F) Estimation of the cutoff frequency of the 2L-OFET. Gain is defined as 20 log($\Delta I_D/\Delta I_G$), where ΔI_G and ΔI_D are the amplitudes of the output gate and drain currents, respectively. The cutoff frequency is extracted from the frequency of the gain equal to zero. Reproduced with permession [26].

In another study the same authors reported the fabrication of large-area OSSC domains with controlled layer-number thicknesses between 5.3 nm to 80 nm by adjusting the processing parameters of a blade-coating technique. The films are composed of large OSSC domains, each of which exhibits a clear change in brightness on rotating the film about an axis perpendicular to the substrate in the crossed polarized microscope analyses [27]. In 2018, Hasegawa *et al*. introduced a novel concept of blade coating method to grow of wafer-scale, over a six-inch size scale single molecular bilayers (SMB), based upon the idea of geometrical frustration, which can effectively suppress the interlayer stacking while maintaining the assembly of the intra-layer, which originates from the strong intermolecular interactions between π-conjugated molecules [28]. These SMBs are produced easily and reproducibly by a simple blade-coating technique based on a variety of extended π-electron framework substituted by variable length of alkyl chains, and is enabled by introducing the effect of geometrical frustration by chain length disorder on the supramolecular layered crystallization in the solution phase under ambient conditions, Figure 5. The SMBs afford OTFT device characteristics exceeding those of amorphous silicon devices.

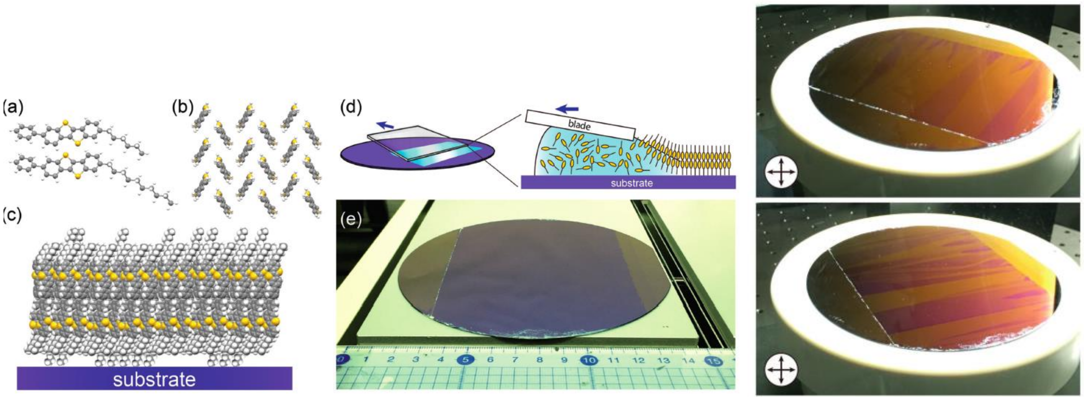

Figure 5. Wafer-scale SMB formation. a) Schematic for two kinds of OSCs with different alkyl chain lengths. b) Molecular packing motif of OSC within the molecular layer viewed along molecular long axes.

c) Schematic for layered mixed crystal of OSC that embraces alkyl chain length disorder. d) Schematic representation of the blade-coating technique. e) A photograph of a six-inch wafer-scale SMB produced using a mixed solution of OSC with different alkyl chain lengths, C10 and C6. The highly uniform film area was as large as 100 cm^2. Right, Observed images for the wafer-scale SMB. The stage is rotated 45 ° from top panel to bottum panel. Monocolored domains with sizes of about 100 μm X 10 μm are neighbored with each other within the film, and the brightness of respective domains changes from bright to dark or vice versa by rotating the stage. Produced with permission [28].

In crystallogenesis, it is well known that good quality crystals are obtained when the interface is flat, where the irregular interface could lead to undesirable defects, such as gas bubble entrapment, strains, cracks, inhomogeneous of impurities, and low-angle grain boundaries [29]. Based on these observations and analyses, Chan and co-workers proposed an original approach to inch-scale synthesis of highly oriented C8-BTBT OSSCs by nucleation seed-controlled shearing method (NSCS) [30]. The critical feature of NSCS method lies in the pre-deposited crystal domains developed by first shearing, which has an important role in guiding the further nucleation of the sequential molecules in the second shearing, Figure 6. The authors believe that the orientation of the seeding crystal has a critical role in providing an easier nucleation path and a well-ordered crystal growth by reducing the nucleation energy barrier, suppressing the random and spontaneous nucleation as well as the crystal growth processes in the this method. The OFETs based on the inch-scale OSSC show good uniformity and high yield with a low trap state density, and the highest mobility is up to 14.9 cm^2 V^{-1} s^{-1}. They believe the mechanism of introduction of crystal seeds with specific orientation is a valuable key for the development of a well-ordered OSSCs and large-scale manufacturing of OSCs. The NSCS crystal growth approach would open the avenue for practical application of OFETs in large-area sensors or backplanes of displays through roll-to-roll or direct printing mass production.

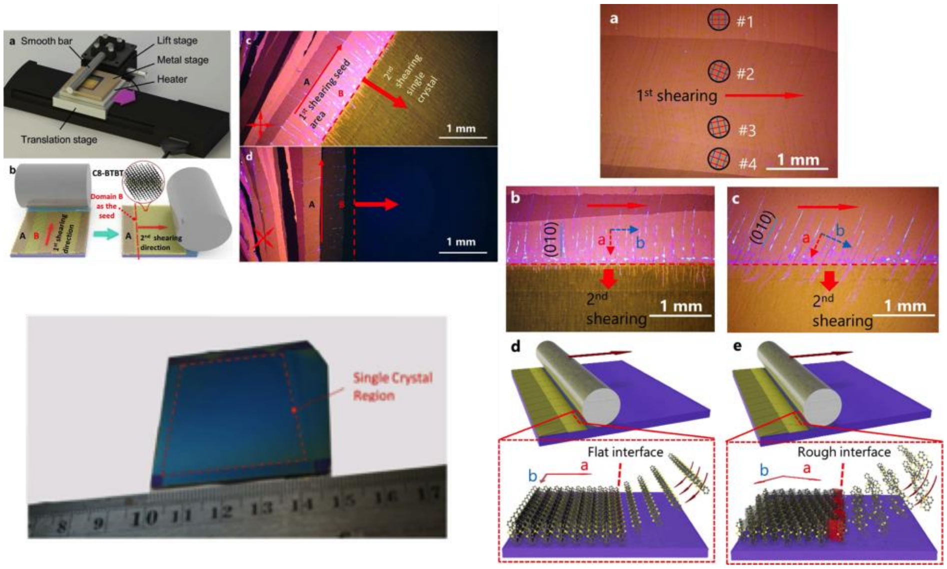

Figure 6. Top left (a) Experimental setup for coating OSCs. (b) Schematic diagram for NSCS method, red arrows indicate shearing directions and dash line is where the second shearing begins. Crystal domain A and B have different molecular orientation deposited by first shearing process and crystal domain B is chosen as the seed for the second shearing process. (c, d) Polarized OM images of organic crystal sample coated by NSCS, the red arrows indicate shearing directions, and dash lines indicate the start of second shearing. Bottom left, photo of the large OSSC with the size around 2 inch X 2 inch. Right, two cases of OSSC from second shearing. (a) Crystals and their orientations by first time shearing. The orientations are determined by cracks on the crystals and colors under polarized OM. Circular symbols are used to represent the orientation of the crystals, where red parallel lines represent the (100) plane and blue parallel lines represent the (010) plane. (b) The polarized OM image of the start part of a large crystal nucleated from similar crystal domain #1 in (a), with crystal growth following the molecular orientation in seed crystal. (c) The polarized OM images of the starting point of a large crystal nucleated from similar crystal domain #2 in (a), with a gradual shift of orientation observed. (d) The schematic diagram of sequential crystal growth follows the flat nucleation seed crystal in the NSCS method. (e) The schematic diagram of asymmetric crystal growth caused by an irregular interface between the seed crystal and the solution. Reproduced with permission [30].

To improuve current understanding of the crystallization at the contact line, Peng *et al.* used finite-element in their study, that takes into consideration fluid dynamics, heat transfer and mass diffusion to simulate the solution shearing of C10-DNTT [31]. The solution substrate contact angle and the substrate temperature were found to be crucial to the crystal deposition. Based on the model simulation, an optimized shearing speed is obtained which is proven through experiments. The shearing speed for optimal morphology was then calculated, assuming that the optimal morphology is attained when the shearing speed matches with the evaporation rate. If the shearing speed significantly deviates from the optimal values, the crystal morphology changes from the polycrystalline to the discontinuous. Similar conclusions have recently been drawn from the model developed by Janneck *et al.* who proposed a model to predict the equilibrium front evaporation speed where the edge of a drop of solvent is receding under the influence of mass loss by evaporation [32]. They showed that films coated at different substrate temperatures, solvents, and OSCs systematically show superior morphology and electrical characteristics when the coating speed is equal to the predicted one. This model is generally applicable, to determine the best coating speed for many solvents and meniscus guided techniques, operated with low shear forces. During solution shearing, the Marangoni flow, widely known as an evaporation-driven convection phenomenon, induced by a temperature-dependent surface-tension gradient near the meniscus line shows negative effects on the deposited films and thickness inhomogeneity. It has been reported in many studies that the addition of co-solvents that can reduce the surface tension gradient in the coating layer during solvent evaporation can prevent the thickness inhomogeneity [33], [34]. Based on this strategy, Chan and co-workers demonstrated that by modifying the gradient of surface tension with different combinations of solvents, the mass transport of molecules is much more favorable, which largely enhances the deposition rate, reduces organic crystal thickness, enlarges grain sizes, and improves coverage, as demonstrated in transmission electron microscopy (TEM) image, Figure 7 [35]. Therfore, to overcome the negative Marangoni effect induced by temperature gradient, they used a blend of solvents. With blended solvents, a surface tension gradient is generated at the liquid–air interface to assist the transport of organic molecules towards the contact line. The ortho-dichlorobenzene (o-DCB) was chosen, because it has higher surface tension and lower volatility than m-xylene as the second solvent. When the mixed solvent is used, a higher concentration zone of o-DCB is formed at the contact line because it is less volatile than m-xylene and it is difficult to replenish from the inner part of solution. The higher surface tension properties of the o-DCB pull the organic molecules toward the contact line from m-xylene rich region with lower surface tension. With this extra path for the OSCs, the shearing speed can be increased to match the enhancement of the molecular transport. The shearing speed of the modified bar-coating method is increased five fold up to 1 mm s^{-1}, and the deposited C8-BTBT OFET active layer with a few monolayers thickness can achieve a carrier mobility up to 16.0 cm^2 V^{-1} s^{-1} with a very good uniformity over an area of 2 × 2 cm^2. The same observation was recently reported by Dong *et al.*, who achieved the fabrication of highly oriented C8-BTBT crystalline thin films by the Marangoni effect-controlled oriented growth [36]. Thereby the substrate is dipped into a blend of toluene and carbon tetrachloride containing C8-BTBT, and then lifted from the liquid. With the evaporation of the solvent, the “coffee ring” effect makes C8-BTBT molecules deposited on the upper edge of the substrate, while the Marangoni effect causes a movement of the C8-BTBT molecules away from the upper edge. The balance of these two effects favours the production of a uniform C8-BTBT film on the substrate during the evaporation of the solution.

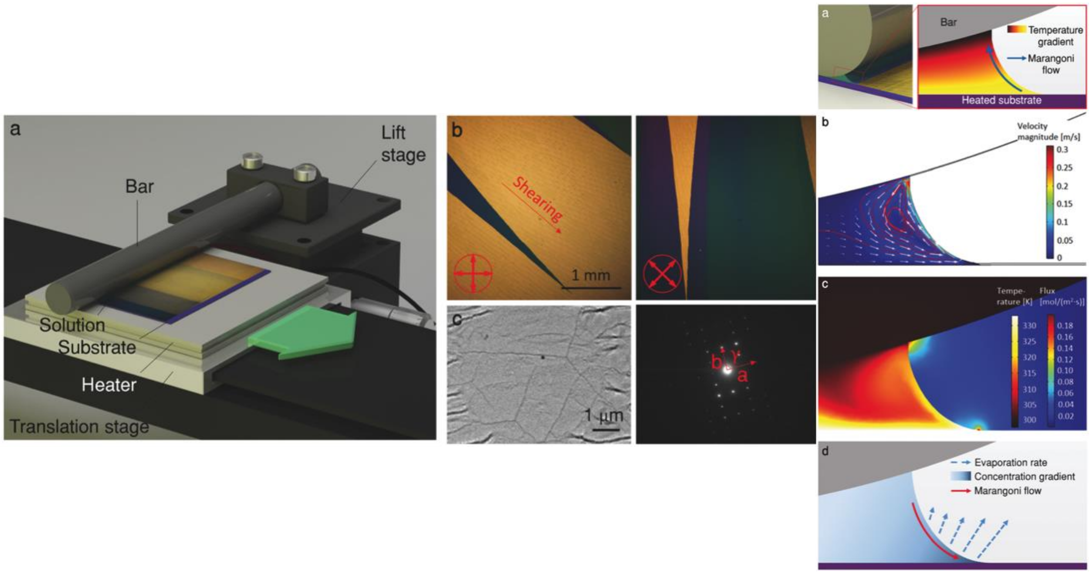

Figure 7. Left, a) Schematic diagram of crystals deposited by bar-coating method. b) Polarized OM images of C8-BTBT crystal deposited at 200 µm s^{-1}. c) TEM image of crystal film and its corresponding SAED

result. Right, a) Mechanism of temperature-gradient-induced Marangoni flow. b) Simulation results of velocity distribution, and c) temperature and evaporation flux in *m*-xylene during shearing. d) Mechanism of concentration-gradient-induced Marangoni flow by blending *m*-xylene with *o*-DCB. Reproduced with permission [35].

However, under the same preparation conditions, the Marangoni flow cannot drive the spontaneous alignment of the polymer and the polymer molecules often require higher bar moving speeds. At the same time, the surface of the bar is entangled with thin wires, and the gap between the thin wires is more likely to cause capillary phenomenon, which is more advantageous for aligning the molecular orientation. Liu et al. developed a bar-coating method to prepare large-area oriented ambipolar copolymer of fluorinated isoindigo derivatives (PFIBI-BT) through Landau–Levich process in air. An uniform oriented few-layer polymers of A4 size (210 mm X 297 mm) can be obtained on the glass substrate within two seconds [37]. Because of the highly ordered grains and well-aligned edge-on molecules in thinner semiconducting films, the ambipolar OFETs showed a hole mobility up to 5.5 $cm^2 V^{-1} s^{-1}$ and an electron mobility up to 4.5 $cm^2 V^{-1} s^{-1}$. The gain values of the inverter are as high as 174 at positive voltage and 143 at negative voltage, respectively, which are among the highest results of inverters composed of bipolar polymer transistors.

Polymorphism is commonly encountered in organic materials. Different polymorphs, even with the slightest change in the molecular packing can have a huge impact on their electronic properties. Therefore, accessing metastable polymorphs is an emerging approach for fabrication of high device performance. Previous studies have demonstrated that solution shearing process conditions induce polymorphism in the crystal packing. For instance, Giri *et al.* found metastable packing of doctor bladed thin films of TIPS-pentacene (TIPS-PEN), and the authors attributed the phenomenon to nanoscale vertical confinement observed during solution shearing [38]. Thin film confinement was also explored by Diao *et al.* to successfully stabilize highly metastable polymorphs of TIPS-PEN at ambient conditions for structural and charge transport studies [39]. Mas-Torrent *et al.* recently demonstrated that varying the deposition parameters, speed, temperature, and solution formulation (i.e., semiconductor/binder polymer ratio) during the deposition of the dibenzo-tetrathiafulvalene (DB-TTF) blended with polystyrene (PS) by bar-assisted meniscus-shearing method can lead to the formation of either the kinetic or the thermodynamic polymorph, as shown in OM images Figure 8 [40]. Thermodynamically stable α-phase was obtained at 1 mm·s^{-1}, whereas the kinetic γ-phase was formed at higher coating speeds. The surface morphology of the films was investigated and three different morphologies were observed depending on the coating speed. At a low coating speed (1 mm·s^{-1}) where the thickness and roughness were higher and the domains were smaller because of the high number of nucleation points giving long but very thin crystallites. The coating speeds ranging from 3 to 10 mm·s^{-1} gave rise to very smooth and thin films characterized by large crystallites. Finally, in the region with coating speeds above 10 mm·s^{-1}, the films were thicker and the crystallite size domain was smaller. The best device performance was realized in an intermediate deposition regime between capillary and viscous drag regimes, where thinner and smoother films with larger crystalline domains were formed.

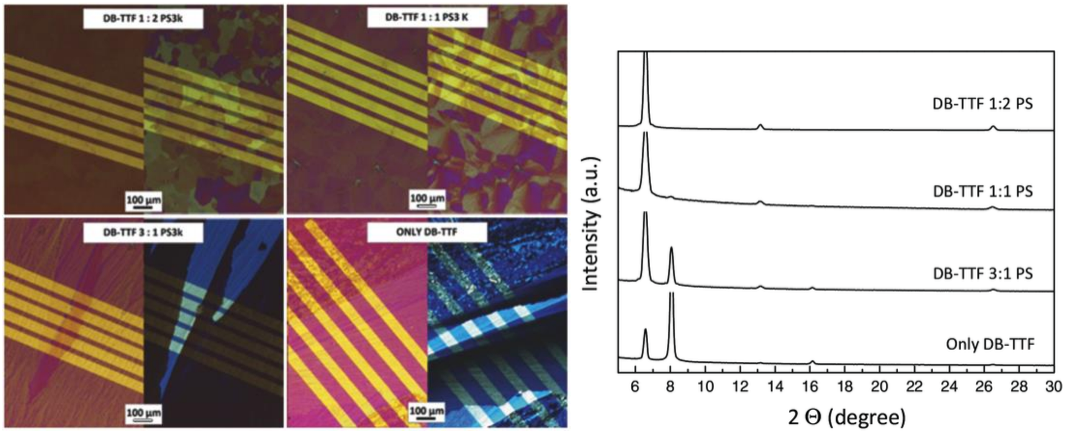

Figure 8. OM images of DB-TTF/PS thin films with different OSC: binder polymer ratio deposited at 105 °C at 7.5 mm s^{-1}. For each formulation non-polarized (left) and polarized (right) images are depicted. Right, XRD diffractograms of DB-TTF/PS thin films with different OSC: binder polymer ratio deposited at 105 °C and 7.5 mm s^{-1}. Produced with permission [40].

The same authors reported a comprehensive study on the fabrication of OFETs using blends of four benchmark OSCs with PS and demonstrated that applying the same formulation and experimental conditions for printing them, highly reproducible and uniform crystalline films exhibiting high OFET performance were successfully achieved. TIPS-PEN, 2,8-Difluoro-5,11-

bis(triethylsilylethynyl)anthradithiophene; (diF-TES-ADT), and C8-BTBT OSCs grow forming spherulitic films with no preferential orientation relative to the shearing direction. On the contrary, DT-TTF films are formed by several millimeter long domains grown along the shearing direction, Figure 9 [41].

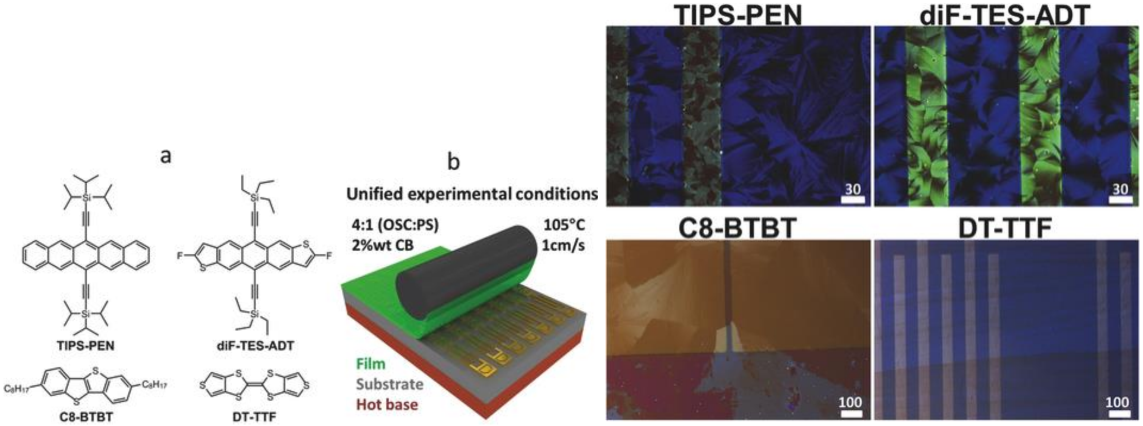

Figure 9. Left, Molecular structures of the OSCs investigated. b) Schematic illustration of the bar-assisted meniscus-shearing method coating technique together with the experimental conditions used. Right, polarized OM images of TIPS-PEN, diF-TES-ADT, C8-BTBT, and DT-TTF thin films. Scale bar: 30 and 100 μm for the upper and lower images, respectively. Produced with permission [41].

The growth of OSC thin films on the substrate surface is highly affected by the local surface energy. By selective control of the surface energy at different areas of the substrate, it would be possible to form patterned OSC regions during the deposition process. Park and co-workers developed a facile strategy to pattern OSC crystals during blade coating by fabricating alternating solvent wetting/dewetting lines on the substrates, where the small-molecule crystals grew only in the wetting regions, Figure 10. They demonstrated the use of hydrophobic UV-curable polyurethane acrylate (PUA) for easily fabricating hydrophobic linear patterns on a hydrophilic surface via one-step photo-curing. PUA precursors diluted in toluene were spin-coated to form thin films on SiO_2 substrates, and the films were selectively exposed to UV irradiation to yield alternating PUA and SiO_2 lines on the surface. Owing to the hydrophobic nature of PUA, the TIPS-PEN/PS blend solution only wetted the hydrophilic SiO_2 regions during blade coating, and thus they were able to produce patterns of linear TIPS-PEN crystals of various widths. Crystal analysis tools revealed that the crystallinity and alignment of the crystals depended on the pattern widths [42].

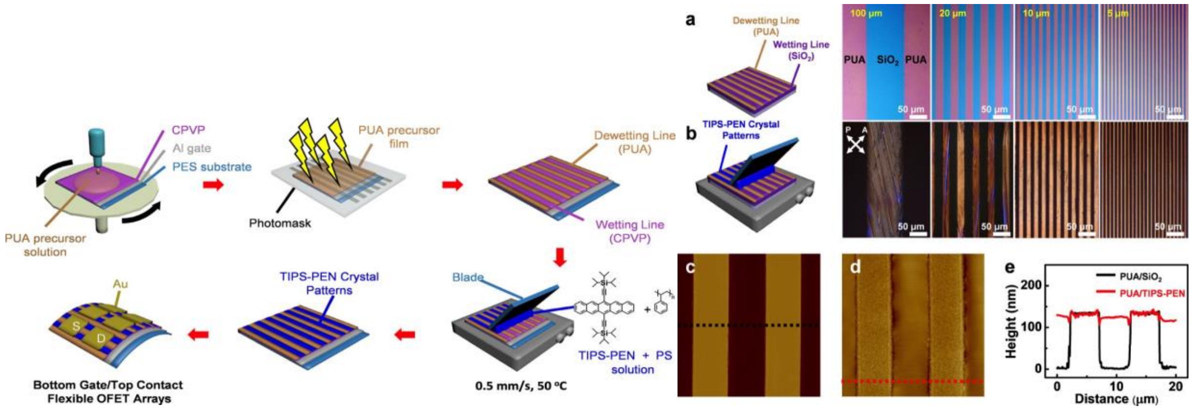

Figure 10. Schematic diagram of microcontrolled blade coating for preparation of flexible TIPS-PEN OFET arrays. Hydrophobic PUA line patterns were fabricated onto the precursors. Blade coating of the TIPS-PEN/PS blend solution was performed along the PUA lines. Left, OM images of various PUA/SiO_2 substrates. (b) Polarized OM images of TIPS-PEN crystals of various widths. (c,d) AFM topographies of PUA/SiO_2 and PUA/TIPS-PEN substrates and (e) their cross-sectional height profiles. Produced with permission [42].

Recently, solution shearing was utilized to fabricate tunable nanoporous OSC thin films where the pore sizes can be tuned in the insulating layer template. The tunable and relatively uniform pores in the template layer ranging from 50 to 700 nm were obtained by altering the ratio of 4,4-(hexafluoroisopropylidene)-diphthalic anhydride and poly(4-vinylphenol) [43]. The poly(diketopyrrolopyrrolethiophene-thieno[3,2,b]thiophene-thiophene), (DPP2T-TT) and C8-BTBT semiconductors were deposited on the template as the active layer for sensors for volatile organic compounds such as ammonia and formaldehyde. Flexible sensor chip for monitoring breath ammonia was demonstrated with unprecedented ultras-sensitivity, ultrafast, selective chemical sensing below the 1 ppb level. According to the authors, the key to their method is to direct the semiconductor deposition using a nanoporous insulating layer serving as the template, which can be fabricated over a large area via one-step microphase separation during processing. In a recent study, the same group demonstrated a large modulation of charge carrier mobility via channel doping without disrupting the molecular ordering and thin film morphology. Central to the method is the introduction of nanopores into the OSC thin films via

MGC method, and subsequent solution deposition of a dopant layer on top of the porous OSC film [44]. The success of such approach is linked to the morphology resulting from vertical phase separation, which has been found to be one of the most common phenomena that exists in all OSCs and widely used to fabricate dual layers in OFET devices. MGC method has shown potential as a processing method of OSC: polymer blend to produce high performances optoelectronic devices [45]. The insulating polymer helps to overcome the common dewetting challenges associated with small-molecule OSC processing. Besides it will also greatly simplify the device fabrication, which is essentially important to reduce the manufacturing cost of organic electronic device commercialization. Qiu *et al.* reported a one-step deposition of bi-functional semiconductor-dielectric layers in OFETs by bar-coating the polymer blend solution on large-area substrates [46]. The vertical phase separation of poly(3-hexylthiophene-2,5-diyl) (P3HT)-top poly(methyl methacrylate) (PMMA)-bottom structure was fabricated in the bar-coating process of the blend solution. The microstructural changes in the ultrathin P3HT films were observed by AFM and TEM. The electrical properties of ultrathin P3HT films on PMMA matrix were measured by fabricating one-step OFETs. Furthermore, the application of this technique was extended to fabricate ultrathin and ultralight OFETs. The transistors were stable when exposed to lights of different wavelengths and different organic solvent vapors. Diao et al. observed significantly different morphology at the free interface as compared to that in the bulk for solution blade coated DPP2T-TT thin films [47]. Revealed by grazing incidence wide-angle X-ray scattering (GIWAXS), AFM, and polarized UV−vis, the polymer fibrils near the top interface exhibit significantly higher degree of alignment than the bulk under most conditions studied. Specifically, well defined polymer fibrils were observed at the top interface, with the long axis and the polymer backbone aligned along the coating direction. In contrast, the bulk fibrils were significantly smaller, either weakly aligned transverse to coating or close to isotropic. This was rationalized in terms of a extensional flow that exists at the top surface due to increasing solvent evaporation rate moving toward the contact line. The same observation was recently reported by Shaw *et al.* who identified three distinct regimes of crystallization behavior for blade-coated diketopyrrolopyrrole−terthiophene copolymer using in situ GIWAXS measurements; revealing a delicate interplay between interface nucleation, solution shear and drying speed [48]. Three separate deposition regimes were observed: the shear-dominate, disorder-dominate, and Landau−Levich−Derjaguin regimes. At low coating speeds, the shear strain imparted upon the solution directly induces polymer alignment, causing an increase in dichroism as a function of coating speed. When solvent evaporation becomes too rapid as coating speeds increase, a decrease in the dichroic ratio is observed before the classical Landau−Levich−Derjaguin regime occurs at the highest coating speeds, resulting in isotropic films. They found that faster coating speeds introduce more disorder into the resulting films because the stochastic nucleation of disordered crystallites at the meniscus air−liquid interface becomes more dominant than substrate mediated nucleation. P(NDI2OD-T2), a copolymer of naphthalene diimide and bithiophene unit, which has higher tendency to aggregate in solution; was blade-coated for OFET applications [49]. Square centimeter large perfectly oriented films with dichroic ratio up to18 and charge transport anisotropies up to 14 were coated from concentrated solutions. They found that: i) the fiber growth direction is along the polymer chain direction, which is in contrast to conventional growth found in P3HT; ii) there is experimental evidence that the P(NDI2OD-T2) film formation can involve liquid-crystalline phases which are frozen when the solvent is completely evaporated, Figure 11.

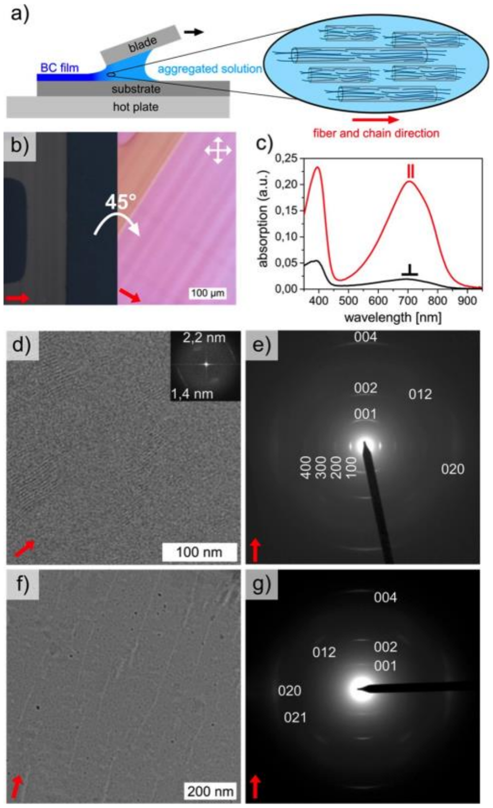

Figure 11. Highly anisotropic P(NDI2OD-T_2) films by blade coating of 20 g L^{-1} chlorobenzene solutions. The red arrows indicate the chain direction. (a) Sketch for blade coating experiment together with nature of the aggregated solution. (b) Polarized OM images of a film coated on a transistor substrate. The substrate is turned around 45° to highlight the birefringence. (c) Polarized optical absorption spectra parallel (red) and perpendicular (black) to the blading direction. (d) HR-TEM image and (e) TEM-ED of films annealed at 220 °C. The inset corresponds to the FFT. (f) TEM-BF image and (g) TEM-ED pattern of a film annealed at 300 °C. Produced with permission [49].

The mechanism by which shear printing can enhance charge transport is not well understood. In recent study, a printing method using natural brushes was adopted to realize direct aggregation control of conjugated polymers and to investigate the interplay between printing parameters, macromolecule backbone alignment and aggregation, and charge transport anisotropy in a conjugated polymer series differing in architecture and electronic structure [50]. This series includes (i) semicrystalline hole-transporting P3HT, (ii) semicrystalline electron transporting P(NDI2OD-T_2), (iii) low-crystallinity hole-transporting PBDTT-FTTE, and (iv) low-crystallinity conducting PEDOT: PSS. The semiconducting films were characterized by a battery of morphology and microstructure analysis techniques and by charge transport measurements. The authors observed that remarkably enhanced mobilities/conductivities, can be achieved by controlled growth of nano-fibril aggregates and by backbone alignment, with good correlation between aggregation and charge transport. However, while shear induced aggregation is important for enhancing charge transport, backbone alignment alone does not guarantee charge transport anisotropy. The correlations between efficient charge transport and aggregation were clearly shown, while mobility and degree of orientation were not always well-correlated. Recently, DeLongchamp *et al.* reported a comprehensive study on the alignment of the polymer backbone during blading [51]. Bulk polymer alignment flipped from perpendicular to the coating direction to parallel as blade speed increased. The anisotropy of top-gate OFET mobility did not agree with the bulk backbone orientation; rather, mobility anisotropy was strongly correlated with the in-plane alignment of the fibrillar morphology at the surface, quantified through AFM image analysis. They also observed a striking periodic, wavelike packing of polymer fibrils at the air interface for low blade speeds and quantified this morphology. While the bulk crystal population for high-speed-coated films was aligned in agreement with optical and AFM results, the crystal population in low-speed films was aligned perpendicular to the coating direction, but with a bi-modal character suggesting conflicting surface and bulk populations. The alignment effect can be additionally enhanced by the external electric filed effect. Bao *et al.* proposed a processing strategy in which an external electric field (E-field) is applied to the coating blade (E-blade) to align polymer chain during solution shearing [52]. A theoretical model based on dielectrophoresis was developed to predicts the alignment process and is used to optimize the conditions of the applied E-field, Figure 12. Using these conditions, more than twofold increase in chain alignment is observed for E-bladed thin films of DPP2T-TT copolymer without affecting other morphological aspects such as film thickness, film coverage, or fiber-like aggregation. A progressive and controlled increase in backbone alignment along the E-field direction, was found for both the crystalline and the amorphous regions of solution-sheared DPP2T-TT thin films due to the increase of the E-field effect at conditions predicted by the model. The coupling between shear strain rate and E-blading is strong for an intermediate coating speed of 0.4 mm s^{-1}, which is slow enough to allow the interaction between the E-field and the drying meniscus and fast enough to prevent strong perpendicular alignment of the polymer along the meniscus pinning line.These results reveal a synergistic alignment effect from both the solution-shearing process and the applied E-field.

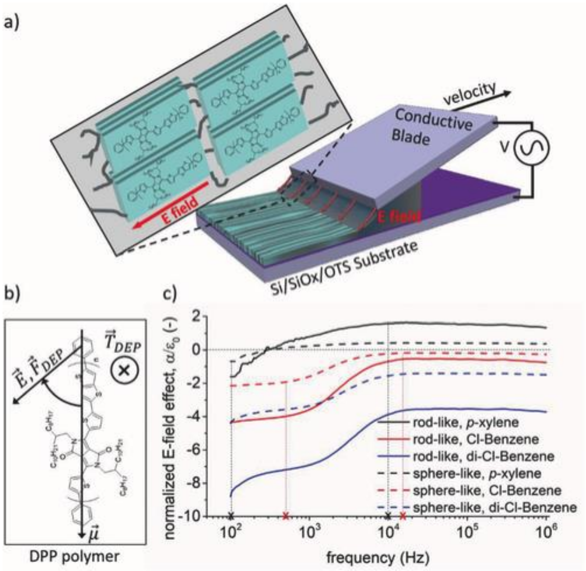

Figure 12. Application of electric field effect to align solution-sheared DPP2T-TT molecules. a) Sketch of the E-blade setup employed: a blade moving at a constant velocity is used to cast the solution sandwiched between the blade and substrate while an electrical potential difference is maintained between them. An E-field is generated along the direction of shearing acting as a brush for the polymer chains. b) Molecular structure of used DPP2T-TT polymer and schematic explaining the physics of the process: dielectrophoresis (DEP) forces (F_{DEP} induces translational motion in the molecules) and torques (T_{DEP} induces the rotation represented by the arc) are expected to act upon the DPP2T-TT molecules (or aggregates), aligning their backbone with the applied E-field direction. c) Estimated normalized E-field effect (polarizability α divided by vacuum permittivity) for DPP2T-TT showing the dependence of α and thus the DEP force and torque on solvent and E-field frequency. Produced with permission [52].

Solution shearing has so far been mainly used for the uniaxial deposition of OSC materials, however, the application of the solution-shearing technique to dielectrics is very limited. In recent work

Haase *et al*. presented an innovative approach for the deposition of ultra-smooth dielectric layers for transistor applications, by solution shearing [53]. They demonstrated also the utility of these layers as ultra-smooth dielectric substrates for further solution-coating steps and compare them to the corresponding spin-coated films. Their work presents an alternative to metal anodization/oxidation protocols that are commonly applied to prepare ultrathin dielectrics to achieve high capacitance values.

III) Periodic deposits and patterned deposition at moving contact lines

In this section, we highlight some of recent publications relating stripe formation during the coating process. Under certain condition the MGC methods such as, dip-coating, bar coating, doctor blade, slot die coating are considered as effective routes to fabricate highly ordered organic crystal arrays by controlling the velocity of the receding contact line, and the experimental conditions. Various striped films have been formed by these techniques. The uniform nanostructured deposits can be prepared over the whole substrate. Even on homogeneous substrates, during solution coating, meniscus instability often arises and results in regular complex morphology of the deposit. These regular patterns result from the motion of the contact line which is dominated by the competition between the pinning force from the solid substrate and the de-pinning force due to the surface tensions. The origin of the pinning force is the mass deposition, and the origin of the de-pinning force is the contact angle and the interfacial tensions at the liquid surface. Various mathematical models have been proposed to describe pattern formation phenomena in experiments, where complex fluids are transferred onto a substrate producing periodic deposits [54]. Doumenc *et al.* proposed a numerical hydrodynamic model for the pinning-depinning process that predicts the deposition of regular line patterns. They obtained periodic patterns whose amplitude was found to depend on the velocity of the moving substrate. Furthermore, they found an empirical law that relates the pinning force and the deposits geometry and concluded that this force controls the wavelength of the periodic patterns. Their model reproduced the evaporative regime and the Landau-Levich regime and obtained only homogeneous deposits. However, by including a solutal Marangoni stress, they obtained patterned deposits in the evaporative regime for certain ranges of the control parameters [55], [56]. Darhuber *et al.* reported the periodic pattern deposition of polymer films from a receding solution meniscus in a horizontal die-coating geometry, by means of experiments and numerical simulations [15]. The substrate speed and the evaporation rate of the solvent were identified as the main control parameters. Periodic deposit patterns, consisting of lines parallel to the receding contact line were observed for certain ranges of the control parameters, as shown in Figure 13.

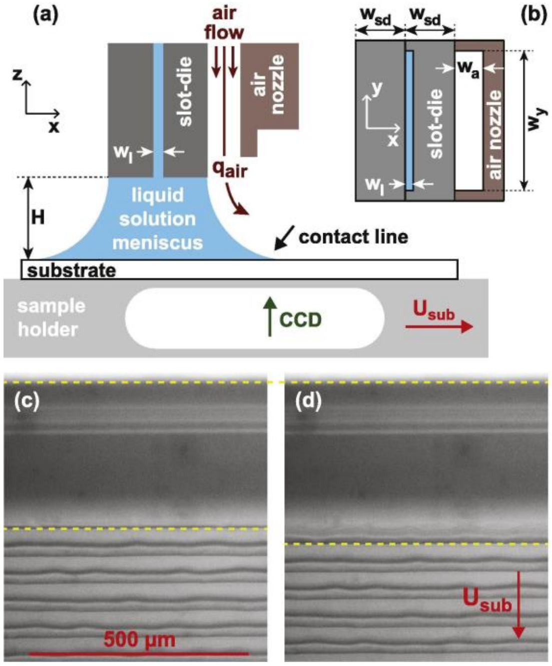

Figure 13. Sketch of the experimental setup. The coating liquid is confined between the slot-die and the substrate. The substrate moves horizontally with a speed underneath the slot-die. Air is pumped through the air nozzle and over the receding meniscus with a flow rate . (b) Bottom view of the slot-die and air nozzle. (c,d) Typical OM images of the receding meniscus. The substrate moves from top to bottom with a speed µm/s. Image (d) was recorded 4 s after (b,c). Produced with permission [15].

The pioneer work on patterned deposits was focused in colloidal suspension of polymers nanoparticles. In the work of Masuda *et al.* particle arrays were deposited into silicon substrate. The particle arrays form periodic lines oriented parallel to the contact line of the liquid meniscus. The width and spacing of the lines could be modulated by controlling the temperature of the solution [57]. Miyahara and co-workers reported well-defined stripe patterns via a convective self-assembly technique. The stripe width depends on particle concentration, withdrawal rate, and surface tension, while the stripe spacing depends on the thickness of stripes, surface tension, and type of substrate [58]. Yabu and Shimomura developed an original method to control mesoscopic patterning from polymer solutions of P3HT and PS, using a homemade set-up similar to doctor blade coater, as shown in Figure 14 [59].

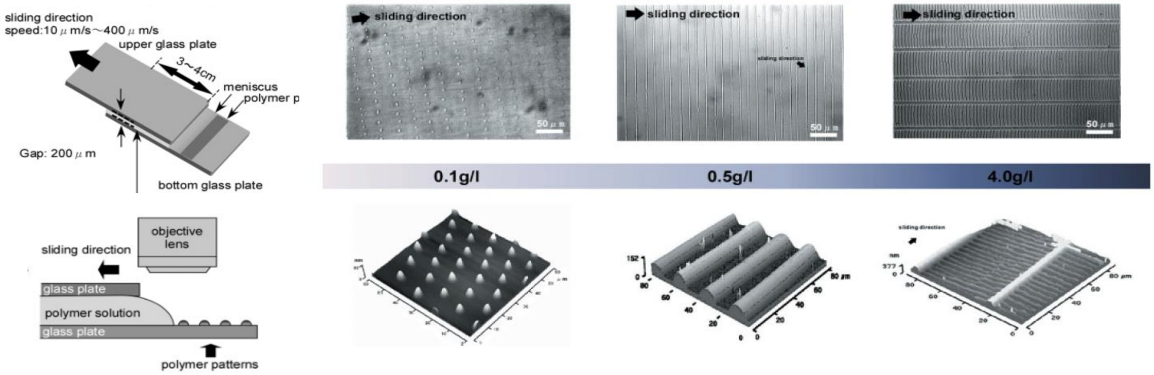

Figure 14. Schematic illustrations of the experimental set-up, and OM images (upper row) and AFM (lower row) of polymer patterns prepared from PS solutions. Produced with permission [59].

A polymer solution was introduced into the gap between two glass plates, and the upper glass was allowed to slid over the lower. The meniscus of the polymer solution allowed the edge of top glass plate and various polymer patterns were formed on the bottom plate. Three types of micrometer scale patterns were observed: dots, stripes, and ladders driven by dewetting, stick-slip motion and fingering instability, respectively. Polymer patterns can be prepared not only on a planar substrate but also on a curved surface. Crosby *et al.* reported a study of the spontaneous, controlled formation of striped patterns of quantum dots of CdSe by flow coating, by regulating the motion of translation stage. Both parallel and crossed multi-component stripe patterns were prepared by controlling the rate and direction of the stage translation, Figure 15 [60].

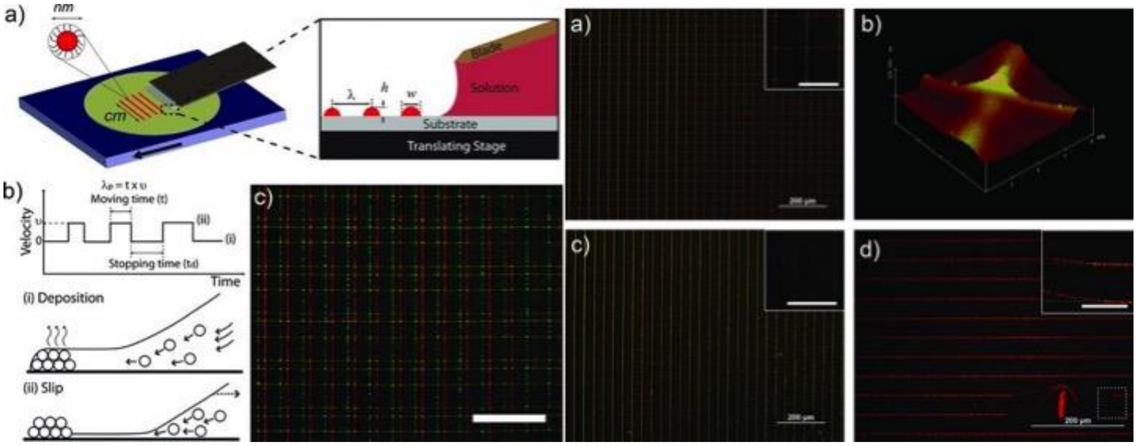

Figure 15. (a) Schematic diagram of the flow-coating apparatus for generating stripe patterns of CdSe on a silicon wafer. (b) The velocity profile of the translation stage for manipulating the stick-and-slip motion of the contact line. Schematic illustration of nanopartcles deposition at intermittent stopping times (i) and slipping of the contact line upon stage translation (ii). (c) A fluorescent microscopy image of grid patterns with homo- or hetero-junction configuration at each crossed point generated by a three step flow-coating process. Scale bar, 200 μm. Produced with permission [60].

As previously discussed in section II, the wetting/dewetting properties of the substrate have been explored to pattern OSC films from micrometer to tens of nanometers range without a predefined template. For example, substrates patterned with alternating regions of hydrophobic and hydrophilic molecular layers result in selective deposition of single-walled semiconducting carbon nanotubes (SWCNTs) into hydrophobic zones and large-area assembly of densely aligned SWCNTs using solution shearing, as shown by Bao *et al*. Meniscus confinement was the key to enabling selective deposition and alignment of SWCNTs [61]. Thus, a silicon wafer was patterned with alternating regions of tridecafluoro-1,1,2,2-tetrahydrooctyl trichlorosilane (solvent-dewetting) and phenyltrichlorosilane (solvent-wetting) self-assembled monolayers, as the shearing blade is moved across the wafer, the meniscus is pinned on the solvent-wetting regions, while less/no pinning occurs on the solvent-dewetting regions. When the contact line is pinned, the evaporation rate is accelerated at the contact line, which causes edge-ward convective flow and transport of both solvent and SWCNTs towards the contact line. As the solvent evaporates, the concentration of SWCNTs at the edge of the contact line increases, resulting in the deposition of SWCNTs on the surface, as shown in Figure 16.

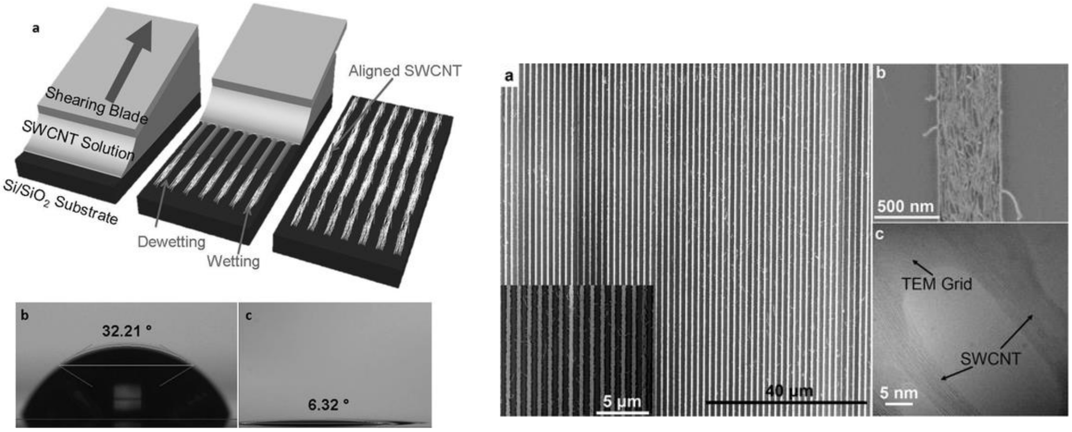

Figure 16. a) Schematic depiction of SWCNT alignment using solution shearing, top left; b,c) Bottom left, contact-angle measurements of toluene on self-assembled monolayer of tridecafluoro-1,1,2,2-tetrahydrooctyl trichlorosilane, (b) and self-assembled monolayer of phenyltrichlorosilane (c), respectively. Right, SEM and TEM images of shear-aligned SWCNTs, a) Large-area SEM image of the shear-aligned SWCNTs on 500 nm wide solvent-wetting regions. The inset is a zoomed-in image of the same area. b) SEM image of a single strip of solvent wetting region showing well-aligned SWCNTs. c) TEM image of a couple of closely packed SWCNT arrays. Produced with permission [61].

Solution processable OSCs promise to allow mass-production of low-cost electronic devices on flexible substrates. Large-scale integrated applications, such as active matrix displays, logic circuits, and sensor arrays, require minimal cross-talk between neighboring devices. Patterning OFETs has been widely used to minimize cross-talk and integrate these OSC crystals into practical devices. Although photolithography method has demonstrated high spatial resolution, and has been widely used to pattern OSCs, easy patterning method compatible with large-scale, heterogeneous integration processes, still poses challenge [62]. It has been shown that solution-shearing techniques are effective methods to produce a large-area well-aligned OSC-arrays with preferential orientation. Lee *et al.* investigated the pattern formation of squarine OSC and found that the nanowires can be assembled into ordered structure on solid substrates either as periodic rings or parallel stripes [63]. The density, length, and periodicity of the nanowire arrays were tuned by controlling the evaporation conditions. The mechanism by which the stripe pattern formation was investiaged. Hence, the silicon substrate was firstly treated with oxygen plasma to make its surface hydrophilic, which limits its wettability towards the hydrophobic dichloromethane. When, the solvent meets the surface at a nonzero contact angle, the contact line is pinned due to surface roughness, Figure 17. The physical phenomena of contact line pinning and solvent evaporation cause the solutes in the droplet to flow toward the contact line (i.e., capillary flow). A higher evaporation rate, the liquid/substrate interface would increase the local concentration of molecules and lead to nucleation of nanowires when a critical concentration is reached. This is behind why most of the nanowires nucleate along the same line and form a nanowire array.

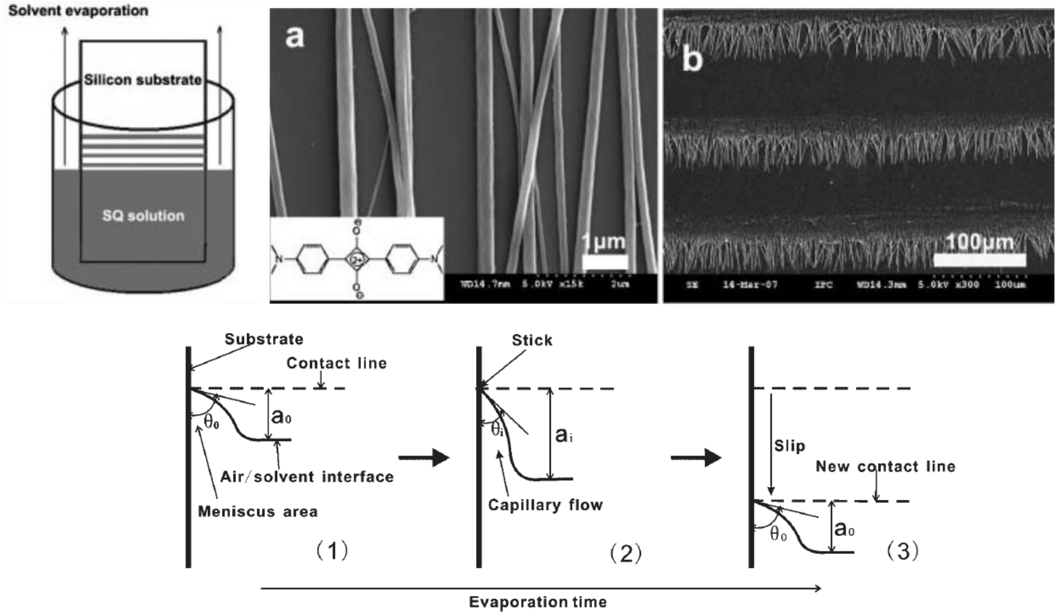

Figure 17. Schematic illustration of dip-coating setup. a) SEM image of the as-prepared nanowires on a silicon substrate. The inset shows the molecular structure of SQ. b) SEM image showing patterning of aligned SQ nanowires. Bottom: stepwise schematic showing the contact line moving process on a vertical substrate induced by solvent evaporation. In the initial stage (1), the contact angle between solvent and substrate is θ_0 and the meniscus height is a_0. 2) As evaporation time elapses, contact angle decreases and meniscus height increases because contact line sticks on the substrate. 3) When meniscus stretches to its maximum, contact line cannot stick but slip to a new position. Thus, the contact angle and meniscus height return to their initial values, respectively. Adapted and produced with permission [63].

Chi *et al.* in a series of recent articles showed that it is possible to precisely control the growth of monolayer to multilayer ultrathin microstripes of OSC, over large areas by tuning the pulling speed in dip-coating process [64], [65]. In 2013, the same group reported optimizing an NH_3 gas sensor with dentritic microstripes of solution-processable OSC. The low-trap dielectric semiconductor interfaces, stripe-like morphology and ultrathin film enable the OFET-sensors to exhibit unprecedented sensitivity with short response/recovery time [66]. In another work, Pei and his co-worker developed a dip-coating method to grow parallel organic nanowire arrays with adjustable length, density and periodicities [67]. By optimizing the stick-slip motion, the solvent evaporation conditions, and the solution concentration, parallel organic nanowire arrays with tunable length and desirable density and periodicity are directly grown and aligned on the substrate. To induce the nanowire self-assembly process at the contact line, the evaporation speed of the solvent has to roughly match the seed growth speed.

In OFETs, the quality of charge transport pathway strongly affects the performance of the device. One effective strategy to efficiently enhance the charge transport pathway is the fabrication of oriented growth of the crystal arrays via an optimized dip-coating method using quick evaporating solvents. In a series of works, Park *et al.* showed that optimized crystals were grown when the rate of input/output flows at the contact line is well-balanced with the substrate lifting rate [68], [69]. This conclusion was supported by optical, crystallographic, morphological, and electrical analysis of TIPS-PEN crystals, as well as by variable-temperature dip-coating experiments with various solvents and lifting rates, Figure 18.

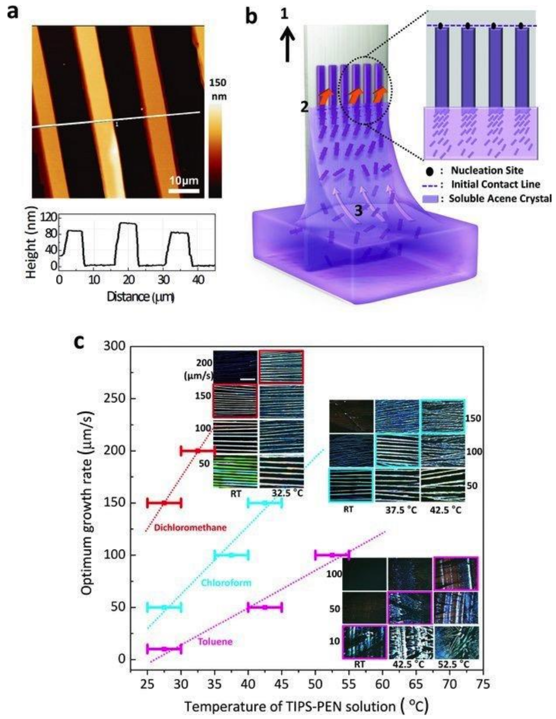

Figure 18. a) An AFM image of the optimally grown TIPS-PEN crystals (in dichloromethane at 150 μm/s) (top) and a height profile of the three adjacent crystals (bottom). b) Simplified schematic illustration of fast evaporation-induced crystal growth, and magnification of the contact line. c) Temperature dependence of the optimum growth rate of TIPS-PEN for the various solvents. The insets show polarized OM images of the TIPS-PEN crystals that correspond to each experimental condition. The scale bar indicates 200 μm. Reproduced with permission [68].

As in the case of dip-coating and as we discussed above, in solution-shearing techniques the meniscus formation and wetting/dewetting aspects are crucial and are influenced by the surface energy of the substrate and the blade. Recent literature has pointed out the impact of the surface energy on film formation and morphology. Bao *et al.* have shown that highly aligned single crystals of TIPS-PEN can be patterned on selectively wetting surfaces using nucleation and solution shearing method [70], [71]. They developed a method that uses differential surface wetting properties combined with solution shearing to pattern and align crystalline domains of OSC. Janneck *et al.* have systematically investigated the effect of substrate surface treatments on the quality of thin crystalline films formed by zone casting, at slow coating speed, that precisely balances meniscus retraction by evaporation, Figure 19 [72]. Surface treatments with good wettability yield low contact angles (typically <5°) leading to continuous and uniform film formation with a morphology that is quite independent from the surface treatment. Solvent surface treatment combinations with higher contact angles lead to unsuccessful coatings, as solvent evaporation at the tip of the meniscus is suppressed, compromising solute supersaturation and precipitation.

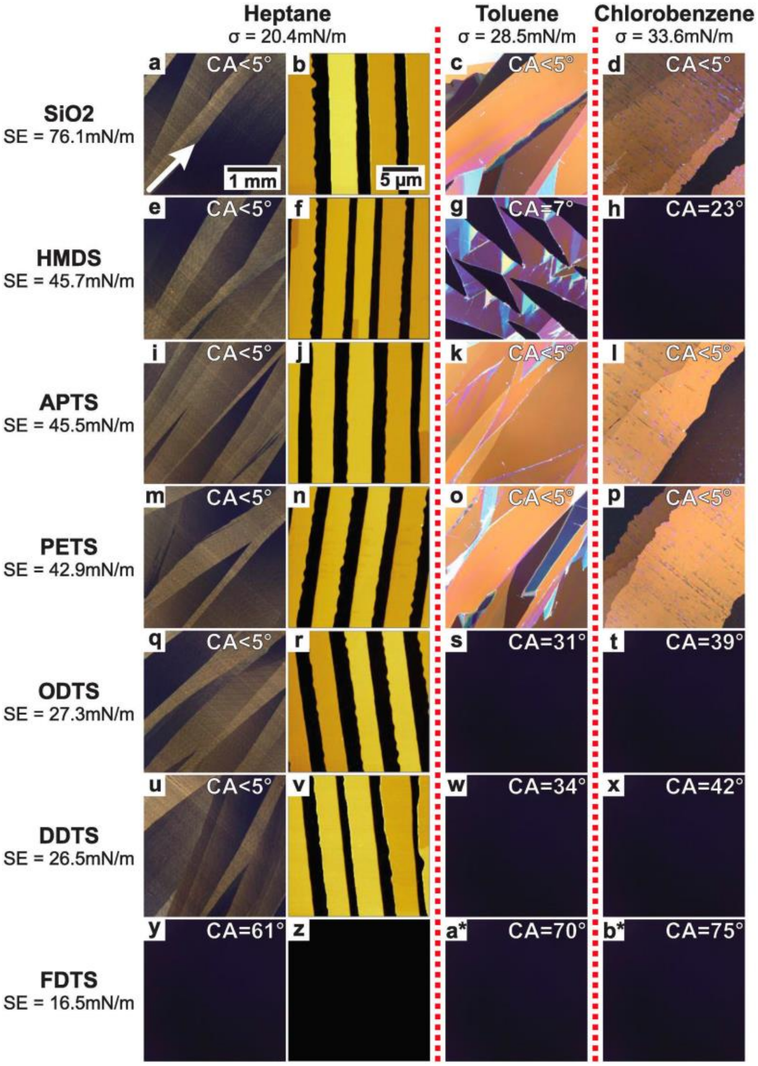

Figure 19. Morphology of C8-BTBT films zone-cast on seven surface treatments with decreasing surface energy (SE). Solutions of the OSc are prepared with heptane, toluene, and chlorobenzene with increasing surface tensions σ. Heptane and toluene solutions are coated at room temperature, chlorobenzene solution was coated at 50 °C. First, third, and fourth column are polarized OM images and second column, shows AFM images z-scale: 35 nm. a) White arrow shows coating direction for the microscopy images. Coating

in AFM images is from bottom to top. CA is the contact angles of the pure solvent on each surface treatment. Depending on the combination of surface treatment with solvent, full, partial, or no coverage is obtained. The morphology of fully covered films is independent of the surface treatment. Reprinted with permission from [72].

The evaporation behavior during the drying process has an important role in controlling the deposit morphology and the alignment of crystals. When the contact line is pinned during drying, the liquid membrane has a fixed contact area so a capillary flow of the solvent occurs from under the contact line to the contact line to replenish the evaporation loss, and this flow transports the solutes to its border. One approach to improve the homogeneity involves the deposition from a blend of solvents to reduce the coffee ring effect. This approach makes use of the evaporation-induced flow, in particular the convective and Marangoni flows that occur during drying. As previously discussed, the Marangoni flow is induced by the surface tension gradient between the contact line and the interior of the liquid membrane from regions with low surface tension to regions with high surface tension. Based on the Marangoni effect induced by blend of solvents, Dong *et al.* fabricated large area aligned ribbon crystals, covering over 60% on 4 cm X 1 cm of the wafer substrate, Figure 20 [73].

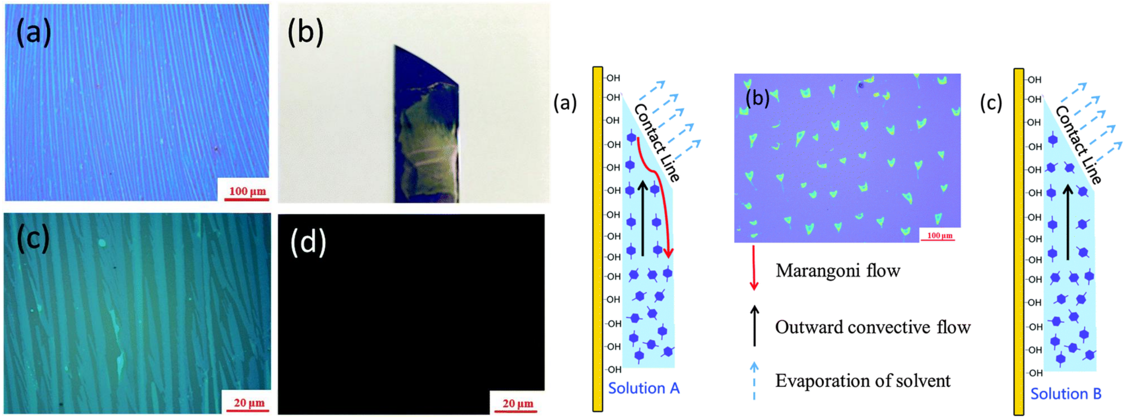

Figure 20. Left, (a) OM image of TIPS-PEN crystals. (b) Picture of the substrate covered with TIPS-PEN crystals. (c) polarized OM image of TIPS-PEN ribbon crystals. (d) polarized OM image of TIPS-PEN ribbon crystals with crossed-polarizers. Right (a) Schematic illustration of TIPS-PEN self-organization when solution A (50 vol% toluene, 50 vol% carbon tetrachloride) is applied. (b) OM image of TIPS-PEN

crystals obtained from the mixed solution composed of toluene and isopropanol (50 vol% toluene, 50 vol% isopropanol). (c) Schematic illustration of TIPS-PEN self-organization when solution B (50 vol% toluene, 50 vol% isopropanol) is applied. Reprinted with permission [73].

The concept of azeotropic mixture was adapted to manipulate the morphology of TIPS-PEN ribbons [74]. Thereby, arrays of crystalline ribbons were obtained with a controllable morphology using dip-coating of binary mixtures of solvents that form azeotropes and exhibit a large contrast in the respective solubility limits, in such a way that the width and spacing of crystalline TIPS-PEN ribbons can be precisely controlled via the speed of dip-coating of an azeotropic binary solvent mixture. The ribbon width monotonically decreases with increasing dip-coating speed. The average ribbon thickness was determined to be approximately of 14 and 65 nm for withdrawing speed of the substrate of U = 0.02 and 0.07 mm/s, respectively, which is consistent with the expected trend that the average film thickness is inversely proportional to the dip-coating speed. As seen in section II, blending OSCs with insulating polymers has been known to be an effective way to fabricate flexible devices. Pisula *et al.* investigated the film formation of dip-coated blends consisting of α,ω-dihexylquaterthiophene (DH4T) or diketopyrrolopyrrole-sexithiophene (DPP6T), and PMMA [75]. They performed a systematic study to understand the influence of the polymer binder on the crystallization of the small molecule OSCs. The effects of the dip-coating speed, weight fraction, and molecular weight of the polymer binder on the film morphology, molecular organization, and electrical properties were investigated. It was found that during the dip-coating of the blends, the polymer binder results in a viscosity gradient at the meniscus drawing more OSCs from solution for mass deposition. The polymer binder solidifies at the bottom layer and decreases the nucleation barrier height of the small molecule OSC. By adjusting the balance between mass transport and crystal growth, the crystal morphology of dip-coated DH4T: PMMA improved from dendritic crystals to long-range aligned crystalline films. During dip-coating, solvent evaporation and substrate withdrawal lead to solute supersaturation at the meniscus, inducing nucleation and crystal growth at the contact line. The dendritic crystals originate from mismatch between the substrate withdrawal and solvent evaporation, leading to an insufficient mass transport for the crystal growth. A vertical phase separation in the dip-coated

DH4T:PMMA film with a top DH4T layer and bottom PMMA layer was reveled using time-of-flight secondary ion mass spectrometry (ToF-SIMS) and X-ray photoelectron spectroscopy analysis, Figure 21.

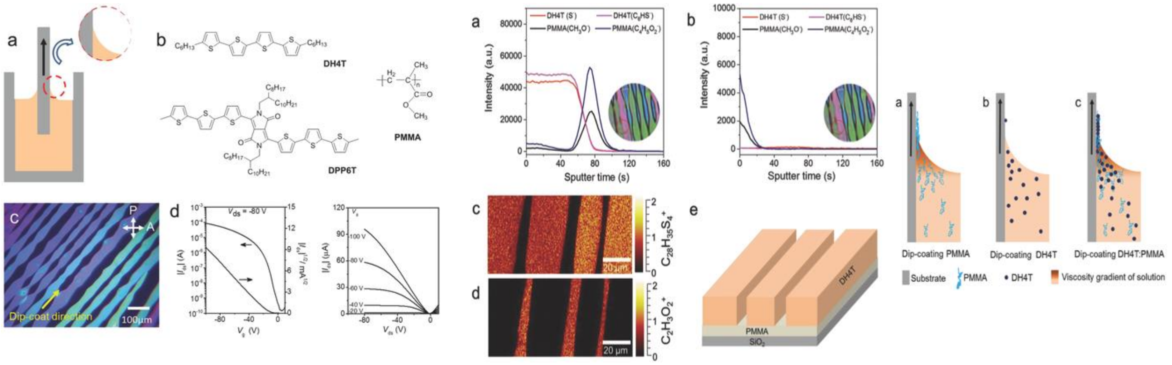

Figure 21. Schematic illustration of the dip-coating process (inset: magnification of meniscus), b) molecular structures of DH4T, DPP6T, and PMMA, c) poalrized OM image, and d) transfer and output characteristics of dip-coated DH4T: PMMA (10%) film. ToF-SIMS depth profiles of dip-coated DH4T: PMMA films reconstructed from the areas indicated by a) circles and b) triangles, lateral distributions of characteristic secondary ion signals of c) DH4T and d) PMMA on the top surface of dip-coated DH4T: PMMA films obtained by ToF-SIMS imaging analysis, and e) schematic cross-section diagram of the DH4T and PMMA distribution in the dip-coated films. Schematic illustration for the dip-coating of a) PMMA, b) DH4T, and c) DH4T: PMMA. Reprinted with permission [75].

As we discussed above, in OFETs, charges are transported near the interface between gate dielectrics and OSCs, therefore the surface parameters of gate dielectrics such as the roughness, surface energy and polarity affect the OSC growth, traps of OSC and control the device performance. Polyimide and poly(4-vinylphenol) (PVP), among many polymeric dielectrics, have been widely studied as a gate insulator for OFETs due to their high chemical stability and good insulation properties, [76]. However, growth of high quality of OSC thin films on polymeric gate dielectric remains challenging. The work by Hu *et al*. reported that polyimide films with tailored surface properties, surface with many strong polar groups (-COOH/-CONH) induce long-range ordered arrangement of OSC on its surface for the formation of high-quality crystalline films with large crystal domain size, [77]. Zhang *et al*. reported a universal, facile, and effective polar surface-confined crystallization (PSCC) method to achieve highly aligned OSSCs on the polymer dielectric, [78]. In this method, patterned PVP surface with alternating polarity difference was used as a growth substrate to guide the aligned growth of OSSCs. Patterned PVP surface with alternating polarity difference was created through selectively oxygen-plasma treatment, as illustrated in Figure 22. UV photolithography was first performed to fabricate aligned photoresist stripes with a width of 2 μm on the surface of PVP layer. Subsequently, the substrate was treated with oxygen plasma to modify the exposed PVP surface between photoresist stripes. After development of the photoresist stripes, alternating oxygen-plasma-treated/untreated regions were formed on the PVP surface. Then, blade-coating of C8-BTBT solution was performed on the patterned PVP surface at room temperature. With the solvent evaporation, molecules are selectively nucleate and crystallize on the patterned PVP surface, generating highly ordered C8-BTBT crystal array at treated PVP areas. As a result of the stronger-polarity PVP surfaces possess higher interaction energy with organic molecules, bringing about the selective aggregation of C8-BTBT molecules and subsequent preferential growth of organic crystals at these regions. In the meanwhile, a geometrical confinement effect of the patterned channels can also prevent multiple nucleation and misaligned molecular packing, enabling the highly aligned growth of C8-BTBT arrays with uniform morphology and unitary crystallographic orientation on the polymer dielectric. The blade-coating speed has crucial influence on the crystal morphology and quality, as shown in Figure 22, on the right. Morphologically, we can distinguish three different regions depending on the coating speed. The first region is at a coating speed less than 80 μm s^{-1} (evaporative regime), where capillary force produced from solvent evaporation would bring about solution collection on the blade front, yielding aggregated crystals on the treated PVP areas. Under an appropriate coating speed, i.e., the speed ranging from 94 to 115 μm s^{-1} (intermediate regime), well-aligned C8-BTBT crystals with uniform morphology can be achieved. However, if the coating speed is higher than 125 μm s^{-1} (Landau−Levich regime, or viscous drag regime), the viscous drag of the PVP surface could only keep a very small amount of solution, resulting in some discrete and small-sized crystals on the treated PVP areas. OFETs made from the C8-BTBT single crystal arrays on flexible substrates exhibit a mobility as high as 2.25 cm^2 V^{-1} s^{-1}, which has surpassed the C8-BTBT polycrystalline film-based flexible devices.

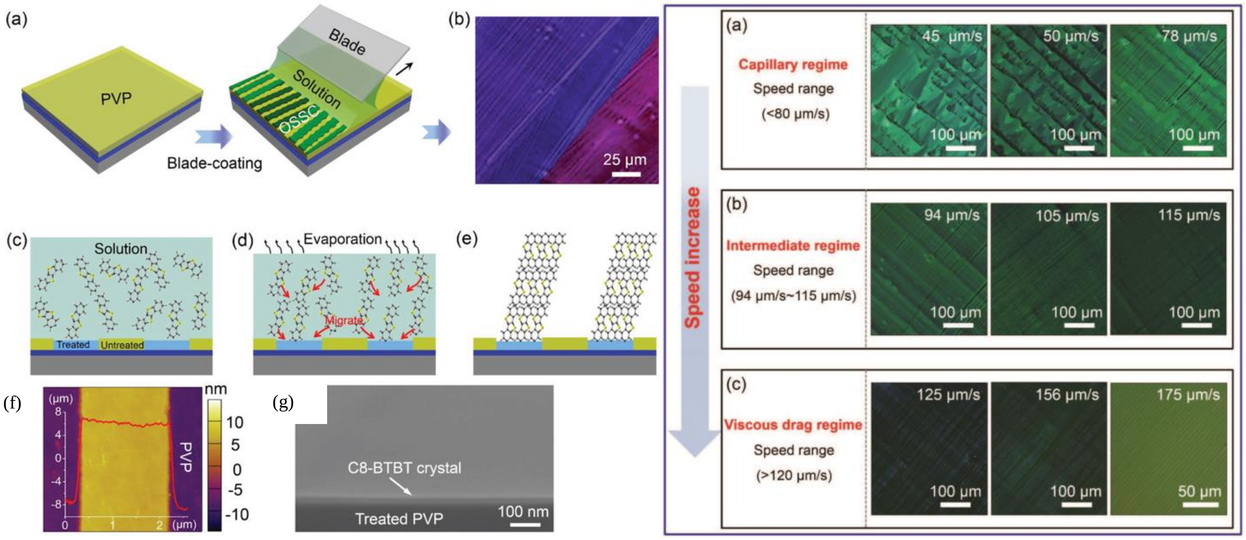

Figure 22. Left a) Schematic illustration of the growth process of the C8-BTBT crystal on untreated PVP surface and b) corresponding cross polarization OM image of the resultant C8-BTBT crystals. c–e) Schematic illustrations of the selective growth mechanism for the C8-BTBT crystal array on treated PVP surface. f) AFM image and height profile of a single C8-BTBT crystal. g) Cross-sectional SEM image of the C8-BTBT crystal. Right, crosse polarization OM images of the blade-coated C8-BTBT crystals prepared under different coating speeds. Reproduced with permission, [78].

In a recent report, Busnaina *et al.* investigated the effect of the pulling speed of the substrate and the solution concentration on the stripe morphologies. Uniform stripe patterns of C8-BTBT parallel to the pulling direction were obtained in a pulling speed range from 5 mm/min to 10 mm/min, due to the stick-slip motion [79]. At lower or higher pulling speeds, nonuniform nucleation at the solution-substrate contact line took place, resulting in a nonuniform film thickness and morphology. Solution concentration governs the amount of solute feeding to the contact line. Continuous stripe patterns were formed only at a high enough solution concentration. Diao *et al.* reported a film-to-stripe morphology transition induced by stick-slip meniscus instability during solution coating of donor−acceptor polymer systems [80]. They observed the coexistence of film and stripe morphologies at the critical coating speed, Figure 23. To understand the morphology transition with meniscus instability, a surface free energy model was proposed. In this model, three changing interfaces, namely the meniscus-free interface, the solvent−substrate interface, and the solvent−deposit interface, where G_{max} represents the surface free energy of the meniscus right before slipping. They hypothesized that morphology transition occurred to lower the maximum system surface free energy G_{max}. With the increase of the coating speed, the meniscus lengthened because of stronger viscous force imposed by the substrate, thus increasing G_{max} of free energy. On the contrary, G_{max}, in stripe deposition, should decrease instead as both the stripe height and the maximum meniscus length continuously shortened with increasing the coating speed. Therefore, at a critical coating speed, where G_{max}, in film deposition, is similar to G_{max}, in stripe deposition, lead to the interchangeable deposition of both film and stripe; lower (higher) than the critical speed, film (stripe) deposition is stable.

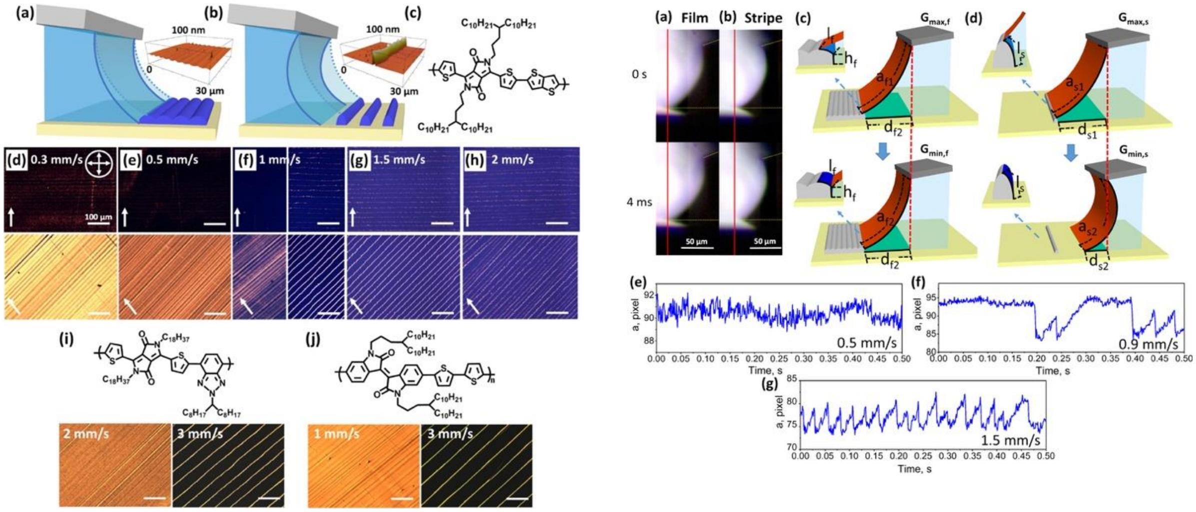

Figure 23. Left, schematics of MGC of DPP2T-TT for (a) film deposition and (b) stripe deposition with stick-slip meniscus motion. AFM image insets represent morphology of the film coated at 0.9 mm/s and stripe coated at 1.5 mm/s coating speed. (c) Molecular structure of DPP2T-TT. (d−h) cross-polarized OM images of DPP2T-TT coated from 5 mg/mL chloroform solution at (d) 0.3, (e) 0.5, (f) 1, (g) 1.5, and (h) 2 mm/s. Deposit morphology transition occurs at 1 mm/s where film and stripe coexist. The crossed arrows indicate the cross polarizer orientation. The top row of images was with the coating direction aligned along a polarization axis of the light, and the bottom row was obtained with the coating direction at 45° from the polarization axis. (i) DPP-BTz molecular structure and morphology transition coated from 5 mg/mL toluene

solution at 2 and 3 mm/s. (j) PII-2T molecular structure and morphology transition coated from 5 mg/mL toluene solution at 1 and 3 mm/s. All scale bars are 100 μm. Right, high-speed imaging of the meniscus motion (side view) comparing (a) film deposition at 0.7 mm/s and (b) stripe deposition at 0.9 mm/s in 4 ms time period. (c,d) Schematics of the meniscus right before and right after slipping (with G_{max} and G_{min}, respectively) during stick-slip motion for (c) film and (d) stripe deposition. The solution-related interfaces contributed to the system surface free energy model were highlighted; they are the meniscus free surface (red), the interface between the ink and the substrate (green), and the interface between the ink and the deposit (blue). The interfaces that remain unchanged between stick and slip are not shown. (e−g) Real-time tracking of the arc length a for (e) film deposition at 0.5 mm/s, (f) film and stripe deposition at 0.9 mm/s, and (g) stripe deposition at 1.5 mm/s. Arc lengths were obtained from the image analysis of each frame captured at 1000 fps with 1 ms intervals. Reproduced with permission [80].

Solution shearing using a micropillar-patterned blade technique has been used to align OSSC domains [8]. The idea was to induce lateral mass transport. This is especially important for unidirectional coating techniques, in which evaporation-driven connective flow occurs mainly along the blade movement direction. In recent study by Park *et al.* a similar principle of flow design was used to pattern the blade, using an inorganic polymer, allylhybridpolycarbosilane [81]. The authors demonstrated that the crystal size of TIPS-PEN can be controlled during solution shearing by tuning the shape and dimensions of the micropillars on the blade. Increasing the size and spacing of the rectangular pillars increases the crystal size, resulting in higher thin film mobility. This phenomenon is attributed to different microstructures inducing varying the degree and density of curvatures in the meniscus line, through which nucleation can be regulated. Finally, they demonstrated that solution shearing can be performed on a curved surface using a curved blade. A double-step method to fabricate high crystalline thin films of OSCs, combining a solution-processed templating layer and a lateral homo-epitaxial growth by a thermal evaporation step is reported by Rolin *et al*. [82]. The first step is the growth of individual, nonconnected single-crystal ribbons from solution by zone-casting coating technique, Figure 24. The second step is the growth of typically ten monolayers of the same OSC by thermal evaporation. The grown layer was found to be epitaxially templated on the crystal seeds of the ribbons, such that it can be considered homo-epitaxial.

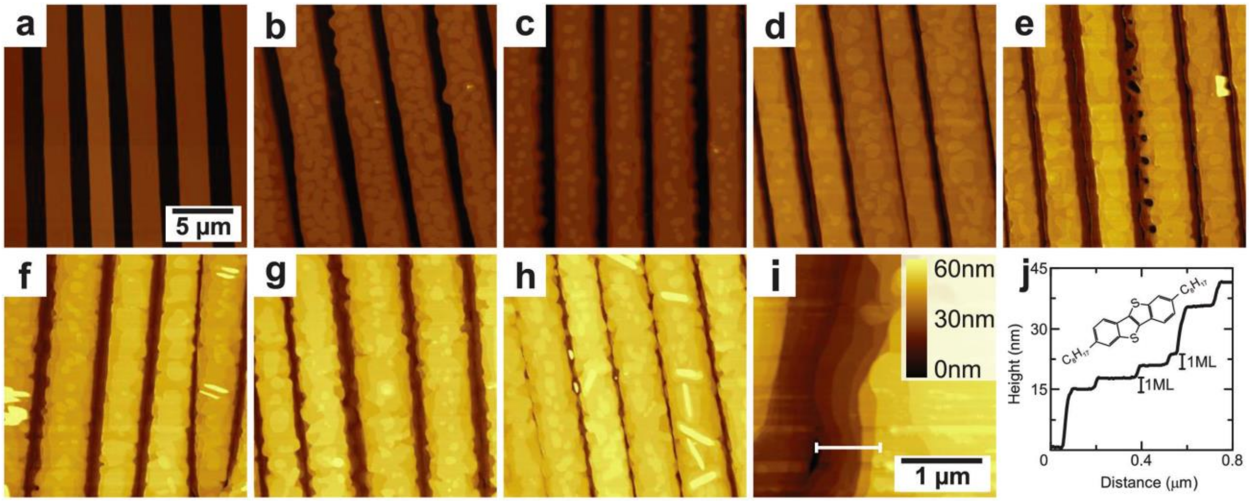

Figure 24. Morphological enhancement by thermal evaporation on a zone-cast templating layer. AFM images of zone-cast OSC ribbons with increasing amount of evaporated OSC monolayers (ML). a) Zone-cast sample only. Zone-cast samples with increasing evaporated thickness: b) 1/2 ML, c) 1 ML, d) 3 ML, e) 5 ML, f) 7 ML, g) 10 ML, h) 20 ML. i) AFM image of the gap area in between two ribbons after evaporation of 7 ML. j) Thickness profile along the profile line of (i). Inset of (j) shows the chemical structure of OSC investigated. Reproduced with permission [82].

The other impressive progress is the improvement of the degree of integration with more sophisticated printed building blocks, such as integrated circuits, photodiodes, etc. enabling fabrication of printing optoelectronic devices. Recently, several studies reported that slot-die coating can be used for the production of highly efficient organic light-emitting diode OLED devices by solution based techniques. A major challenge in solution coating method is coating one layer on top of another can lead to an etching of the bottom layer caused by the solvent of the top layer. One approach to overcome this issue is the orthogonal solvent. However, a low solubility was found to be sufficient to lead to an intermixing of OLED material. Peters *et al*. investigated large area coating techniques for small molecule OLED multilayers under defined drying conditions [83]. Doctor blade and slot die coating were used to coat, host molecule for the emissive and hole transport layers. X-ray photoelectron spectroscopy sputter depth profiling was performed to prove the layer uniformity with sharp interfaces, and the homogeneous elemental distribution of such solution-processed organic multilayers in comparison to well-known evaporated systems. A defined separated interface is created by using orthogonal solvents for two consecutive layers and has been proven by adequate characterization methods. A step toward high-throughput large volume production of flexible OLED devices by solution based roll-to-roll manufacturing technologies was demonstrated, by Abbel *et al*. [84] The development of a roll-to-roll line with two slot-die coating stations is developed which can produce two uniform layers consecutively in a single run, tandem coating, at web speeds up to 30 m/min, Figure 25. After the coating of both hole and electron transporting layers needed for OLED device had been satisfactorily demonstrated, the next step was to apply these materials by R2R techniques also in actual functional devices. By this the devices were then completed by evaporation of an electron injection layer and a cathode and sealed by a thin film encapsulation stack, deposited by plasma deposition of silicon nitride and an inkjet printed organic planarization layer. In addition, patterned deposition of functional materials in the web direction, stripe coating, and perpendicular to it, intermittent coating, has been successfully demonstrated. These patterning techniques offer a strategy that enables complete OLED encapsulation and thus the prevention of premature device degradation by side leakage of moisture and oxygen.

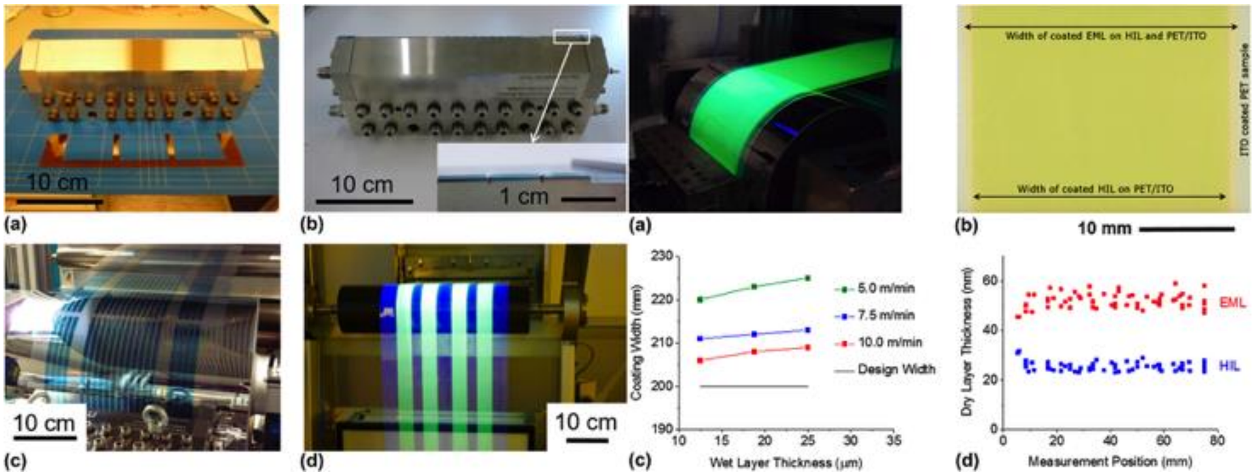

Figure 25. Left, options for R2R stripe coating. (a) Slot-die with shim. (b) Notched slot-die designed for accurate stripe coating and a detail of the notched die lip (inset). (c) Example of well-defined stripe coating

using a notched slot-die, total coating width 240 mm. (d) Stripe coating of EML ink on the HIL under UV illumination. Right, coating of luminescent fluid, visualized by photoluminescence under UV illumination. Coating width 260 mm. (b) A sample of the coated hole and electron transporting materials on PET/ITO at an identical slot-die width (coating speed 5 m/min, coating gap 250 µm). (c) The coated width of luminescent materials ink on V109 PET as a function of the wet layer thickness for different line speeds. (d) The measured coating thickness of the materials on V109 PET within an area of 80 × 80 mm; the target thicknesses were, 30 nm and 60 nm for hole and electron transporting materials, respectively.[84]

A key to the successful manufacturing of solution processed of OLED devices is to construct well-defined electrode stripes with smooth edges, which is of critical importance to avoid crosstalk between neighbouring pixels. Transfer printing and lithographic processing have been employed by several groups to fabricate passive matrix displays [85]. However, additional transfer and lithography steps increase the complexity of the display fabrication, and the reproducibility presents an issue. Guo *et al*. demonstrated four-by-four pixelated colour-tunable tandem OLED devices using a stripe-shaped electrode with a well-defined area using modifying doctor blade solution-deposition method [86]. With an attempt to demonstrate the potential applicability of meniscus guided stripe coatings to fabricate active-matrix OLED display panels, using the slot-die head with µ-tips, Park and co-workers fabricated fine and dense stripes of PEDOT:PSS using a slot-die head with the dual plate [87]. They fabricated 100 stripes with the average width of 227 µm and interstripe width nonuniformity as low as 9.2%. Finally, they have manufactured organic light-emitting diodes atop the conductive PEDOT:PSS stripes and successfully obtained light emission from OLED stripes, Figure 26.

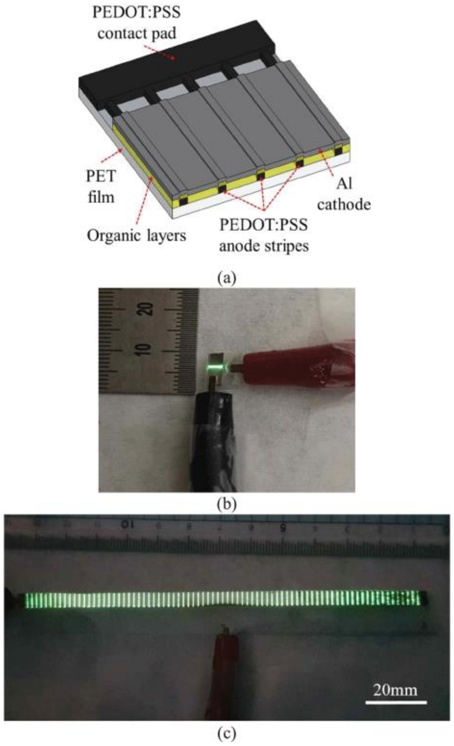

Figure 26. (a) Schematic view of layer structure for the fabrication of OLED stripes. (b) Image of light emission from single OLED stripe at 7 V. (c) Microscopic electroluminescent photograph from multiple (80) OLED stripes at 5 V. Reproduced with permession [87].

The examples highlighted in this section illustrated that MGC method is a promising technique to form highly crystalline, uniaxially oriented, smooth OSC films, for manufacturing superior performance opto-electronic devices. It was shown that during solution coating, the film formation processes and alignment of crystalline domains are critically influenced by a number of processing parameters such as, solvent characteristics (e.g., surface tension, polarity, viscosity, etc.), solvent evaporation rate, temperature, surface tension of substrates, coating speeds, fluid flow, etc. Hence, a fundamental understanding of how processing parameters affect the film morphology and structural orders, crystallinity, grain size and domain orientation, which are relevant to charge transport characteristics needs to be established in order to maximize device performance. Patterning OSC thin films at the nanoscale is a key step in fabricating complex circuits and manufacturing organic electronic devices with reduced costs. Lithography-free patterning of large area fabrication technique with better flexibility, high precision and good uniformity, it is highly desirable. Large-area-compatible techniques such as dip-coating, wire-bar coating, slot-die coating, balde coating have been demonstrated to produce periodic patterns, which are typically produced at low coating speeds. Furthermore, combining solution shearing with hydrophilic/hydrophobic functionalization of the substrates to promote solvent wetting/dewetting lines on the substrates has shown to be an useful approach to pattern OSC regions during the coating process.

IV) A case study: the meniscus guided deposition of P3HT

In this section we investigate the coating speed-dependent film to stripe transition during DBC of P3HT and study in detail this phenomenon in P3HT thin films. We systematically examine the effects of several experimental parameters, including the P3HT concentration, coating speed, solvent evaporation, surface tension of solvents, and nature of substrates, on the stripe width and spacing. The formation of the stripe is attributed to the Marangoni effect. To counterbalance the effect of Marangoni instability, a co-solvent that changes the surface tension dynamically during the coating and drying process is used producing uniform films. We also investigate the synergistic effects of crystallisable co-solvents and solution shearing to generate highly oriented domains of P3HT. The second objective of this section is to study and to characterize the sample surface at different mesoscopic scales using confocal OM, AFM, polarized μ-RAMAN spectroscopy and polarized UV-absorption spectroscopy. All these techniques allow to characterize and control the physical and chemical parameters of the thin polymer films used, as well as to study quantitatively the surface properties topography and chemical composition.

a) Large-scale patterning of P3HT

We start our investigations by studying the ability of DBC to deposit π-conjugated materials such as P3HT. The P3HT was chosen since it is widely used as a model system [88]. P3HT solution in toluene at a concentration of 10 mg/ml was used for film preparation. The detail of the preparation of films by DBC is described in the experimental section. The effects of deposition conditions, additive, and surface nature were analysed to establish their influence on film morphology and properties. We first analysed the effect of key process parameters, such as deposition speed, nature of the substrate and surface energy solvents, on the morphology, physical and functional characteristics of the deposited film. The first important observation was that the thin film topography obtained using DBC is highly reproducible over large surface areas (2×2 cm^2) independent of deposition conditions. A regular array of micrometer-sized P3HT stripes was formed over an area of 2×2 cm^2 on glass substrate when a P3HT solution was deposited at 65 °C with a blading speed of 0.1 mm.s^{-1}. Striped P3HT patterns with 2 cm length were generated all the way over the entire glass substrate. The thickness of patterned film was found to be significantly thicker at the edge of the film, likely due to pinning and depinning events at the contact line during the coating process. In the OM image, Figure 26, well separated P3HT stripes were found to be formed perpendicular to the blading direction. AFM measurements (also reported in Figure 27) showed that the height, width and spacing of the stripes were 50 nm, 3 μm and 3 μm respectively.

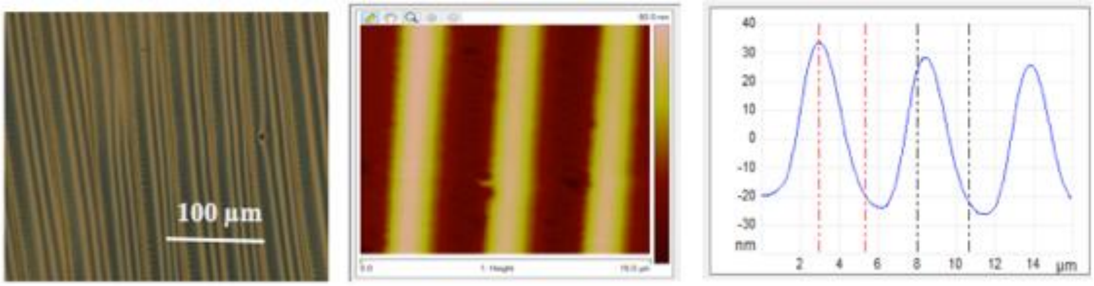

Figure 27. OM image (left), AFM image (center) and AFM profile (right) of a P3HT film forming an array of stripes, fabricated at the blade coating speed of 0.1 mm.s^{-1} at 65 °C. The balding direction is perpendicular to the stripes.

The resulting pattern structure is likely dependent on the meniscus shape of the evaporating solution which is in turn affected by the blade speed. So, the density, height, width, and periodicity of the stripes can be tuned by controlling the blade speed. Consequently, the optimization of the blade speed is important to control the periodicity and the shape of the resulting patterns. We fabricated films at blade-coating speeds ranging between 0.1 and 2 mm.s^{-1}. Optical micrographs of the films in conditions of low (0.1 mm.s^{-1}) and high (2 mm. s^{-1}) blading speeds are shown in Fig. 28. These confirm the patterned films formation at low speed and the fact that the blading speed is an important parameter for the pattern formation. As the blading speed increased from 0.1 to 0.3 mm.s^{-1} the height decreased from 100 nm to 50 nm; the periodicity of the stripes was within the range of 10 to 40 μm. At high blading speed homogeneous unpatterned thin film with a thickness of 20 nm was formed.

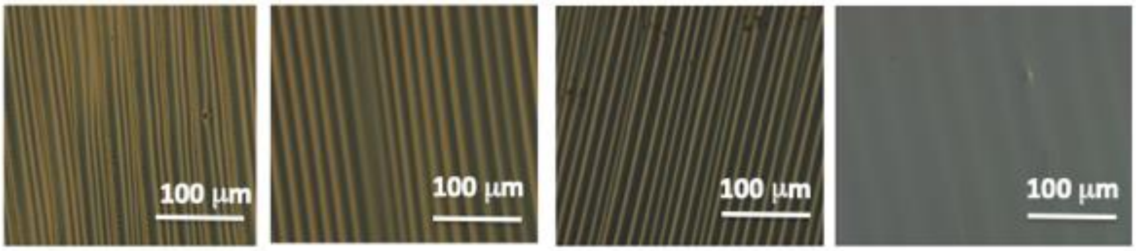

Figure 28. OM images of periodic arrays of stripes on the glass substrate deposited at 65 °C at blade coating speeds of a) 0.1 mm.s^{-1}, b) 0.2 mm.s^{-1}, c) 0.3 mm.s^{-1}, d) 1 mm.s^{-1}.

AFM was performed to image the topography of the patterned P3HT films. The AFM investigations confirm the observations made on larger areas via confocal OM. The AFM images (not shown here) of the patterned P3HT film showed a well-ordered pattern with corresponding profile height. The height and the width of the stripes were, respectively, 100 nm and 35 μm (blading speed of 0.1 mm.s^{-1}) and 50 nm and 6 μm (blading speed of 0.2 mm.s^{-1}). The stripe spacing was within the range of 2 to 10 μm. However, at high blading speed AFM images of P3HT films demonstrate the microstructural evolution from a fibrillar morphology film (cast at a balding speed of 0.6 mm.s^{-1}) to a heterogeneous isotropic film (deposited at a blading speed of 1 mm.s^{-1}).

In order to obtain better precision on the shape of the pattern and to confirm the optical and AFM investigations, a Sloan 3030 Dektak profilometer was used to measure the physical height and width of the P3HT patterned films over all the area of the samples. Because of the size of the 12.5 μm radius stylus tip measurements were found to produce values with accurate vertical resolution, Figure 29. The variation of final thickness with the balding speed are plotted in Figure 30.

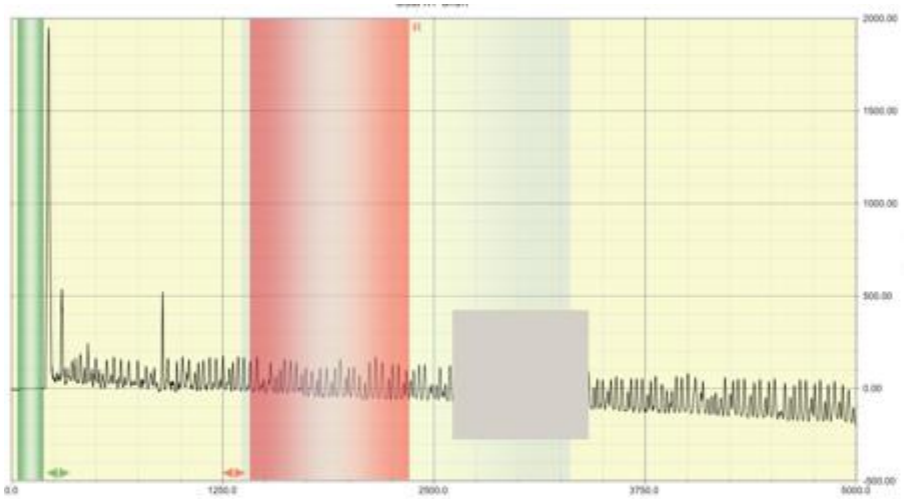

Figure 29. Typical Dektak profile of a P3HT film coated at 0.1 mm.s^{-1} on glass substrate. The height of the stripes was averaged over a distance of few micrometres of the scan on both sides of the transition using the Dektak software. The grey square shows the area from which the height of the stripes was evaluated.

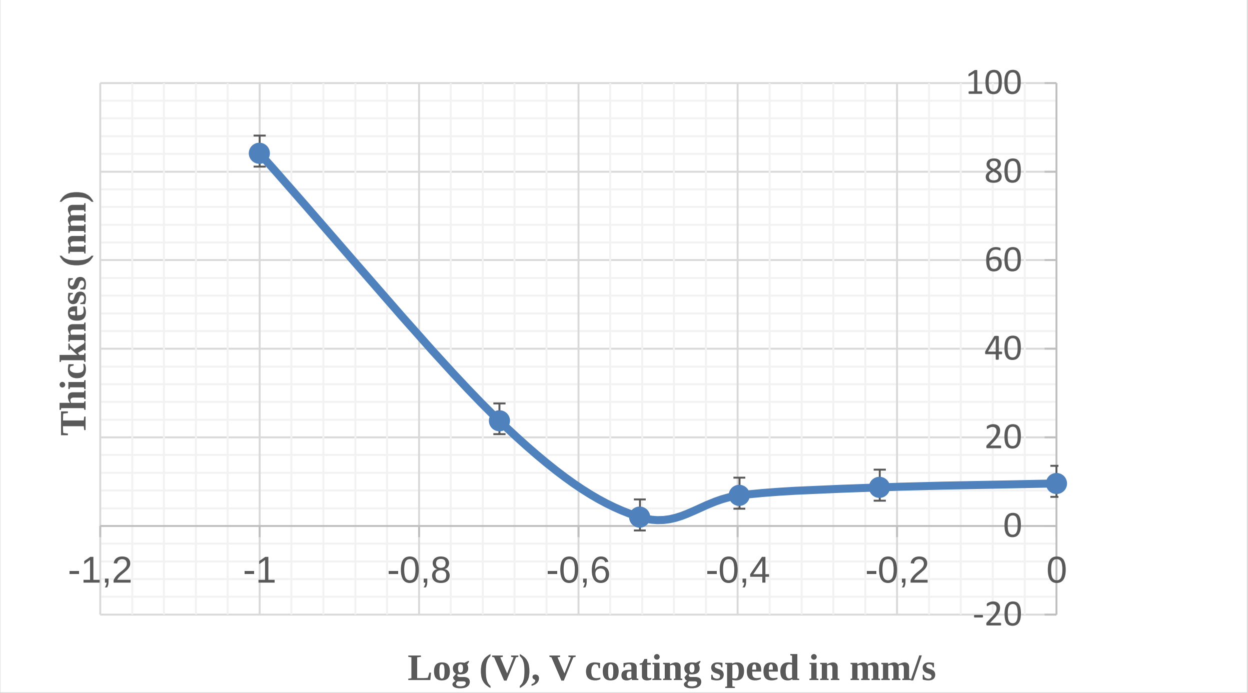

Figure 30. P3HT stripe height as a function of blade-coating speed. The striped film was obtained by coating a P3HT/toluene 10 mg.ml^{-1} solution on glass substrate at a 65 °C preheated substrate. The measured height of the stripes was deduced from Dektak surface profile measurements. The error bars represent the standard deviation of the mean value of the Dektak software data for each sample.

Micro-Raman spectroscopy is a powerful tool for probing the local chemical environment of patterned films. It is likewise widely used as a an important characterization technique for studying molecular semiconducting materials. We used micro-Raman spectroscopy to probe the local environment of the stripes and the grooves. Figure 31 shows the micro-Raman spectra of a stripe and a groove. Both spectra show common features of P3HT: a strong peak around 1445 cm^{-1} assigned to the symmetric C=C stretching mode, accompanied by lower intensity peaks at 1381 cm^{-1}, 1208 cm^{-1}, 1180 cm^{-1}, and 728 cm^{-1} corresponding to the C-C intra-cycle, C-C inter-ring, C-H aromatic, and C-S-C mode respectively.[89] The decrease in the peak intensities indicates that the stripes contain a larger amount of P3HT than the grooves.

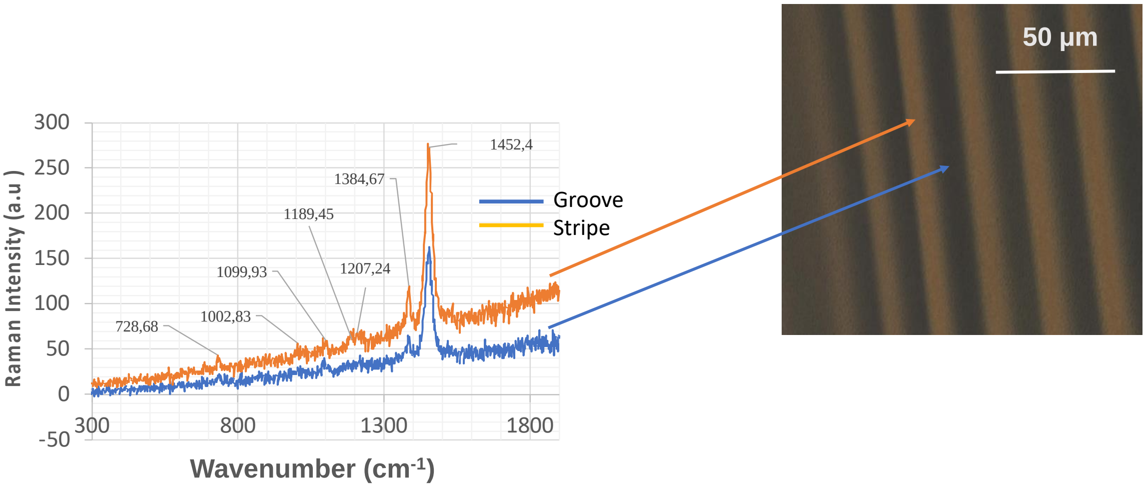

Figure 31. Micro-Raman spectra of P3HT film coated at 0.1 mm.s^{-1} recorded on a groove and a stripe respectively.

Polarized micro-Raman spectroscopy was used to further characterize the degree of the orientation of the P3HT chains in the stripes and the grooves. The Raman spectra with the polarization of the incident light being parallel and perpendicular to the stripe and the groove direction were recorded (not shown here). The strongest signal was detected when the polarization of linearly polarized incident light coincided with stripe direction. Conversely, the weakest signal was detected when the stripe direction made 90° with the incident polarization. Only small changes in the peak intensities when changing polarization were observed in the grooves.

The nature of the substrate surface, the interfacial tension and the physico-chemical properties of the surface are critical factors for film formation and structuration. To further characterize the effect of the nature of the substrate on film patterning we explored four substrates with different surface chemistries, a Al_2O_3 surface (a 50-nm-thin film of aluminium oxide deposited by atomic layer deposition), a SiO_2-silicon wafer, a glass substrate and a hydrophobized silicon surface (a Si-H-silicon wafer). All surfaces were cleaned prior to P3HT deposition following the same protocol. The polymer layer was coated at the speed of 0.2 mm.s^{-1} at 65 °C. Confocal microscopy analysis showed that the P3HT forms a striped pattern on all substrates, see Figure 32. The height and the periodicity of the stripes obtained from the profiles were respectively 120 nm and 45 μm (SiO_2 surface), 24 nm and 10 μm (Al_2O_3 surface), and 24 nm and 25 μm (glass substrate).

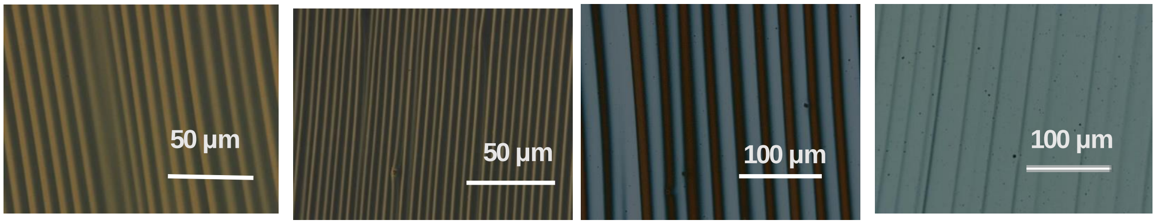

Figure 32. OM images of P3HT coated at the speed of 0.2 mm.s^{-1}at 65°C on different substrates, a) glass substrate, b) SiO_2-silicon wafer, c) Al_2O_3 surface (Al_2O_3 deposited by ALD) and d) hydrophobized Si-H-silicon wafer.

The formation of striped patterns at low blading speeds is caused by stick-slip motion (repeated pinning and depinning) and fingering instability often reported for stripe-patterned particle arrays fabricated using convective assembly methods. In the low blading speed regime, termed also evaporative regime, the solvent first evaporates at the triple contact line and then the coating solution rises to the edge of the meniscus by capillary forces resulting in the pinning of the solution to the substrate. As reported in many studies, the pinning/depinning phenomenon of the contact line leads to the formation of a periodic pattern through successive pinning/depinning of the solution [15]. Figure 33 shows a schematic representation of the pattern formation mechanism induced by the pinning/depinning phenomenon. First, the evaporation of the solvent at the triple contact line induces a thermal or a compositional gradient on the surface that causes convective flows referred to as Bénard-Marangoni convection. The solvent evaporation likewise induces an increase of the concentration of solute at the edge of the meniscus. Then, the coating solution is continuously supplied to the edge of the meniscus by capillary forces. Consequently, the thickness of the coating layer locally increases at the triple contact line leading to the formation of a convex part of the solute. The convex part is continuously moving as the blade moves and gradually separates from the meniscus resulting in the deposition of the polymer onto the substrate. As a result, the edge of the coating solution moves downwards similarly to a receding tide until the next pining occurs by capillary flow. Thus, stripes perpendicular to the blading direction can be formed through repeated pining/depinning of the coating solution at the triple contact line.

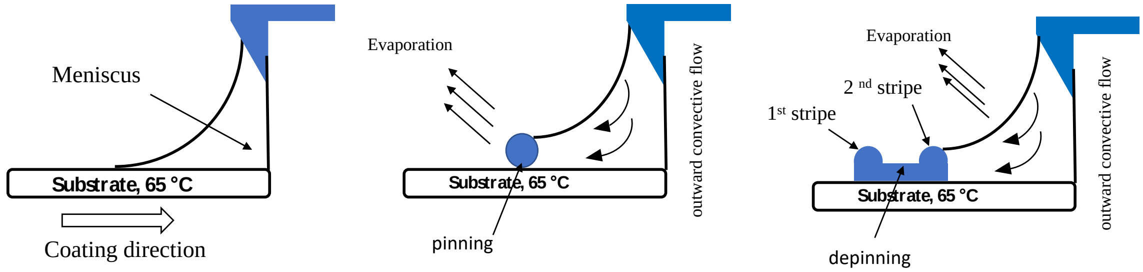

Figure 33. Schematic representation of the formation of the stripe during blading obtained via repetitive pinning-depinning of the contact line. The repeated stick-slip process produces a periodic highly ordered P3HT array.

To verify that the origin of the observed surface patterns is indeed due to Marangoni-type instabilities related to an increase of surface tension in the coating solution with increasing solute concentration, we used a blend of solvents, toluene and o-DCB (80:20 volume ratio) with different surface tensions (28.7 $mN.m^{-1}$ and 35.2 $mN.m^{-1}$ respectively), to assist the pulling of the solution from low-surface-tension regions to high-surface-tension ones. Figure 34 shows the OM image of a film coated at 0.2 $mm.s^{-1}$. Even at low coating speeds the deposited film is uniform, unpatterned and continuous. When the blend of solvent is used, a higher concentration zone of o-DCB is formed at the triple contact line, because o-DCB has higher boiling point than toluene and the evaporated toluene is hard to be replenished from the inner part of solution. So, o-DCB assists in pulling the P3HT toward the contact line from toluene-rich region thanks to its higher surface tension properties.

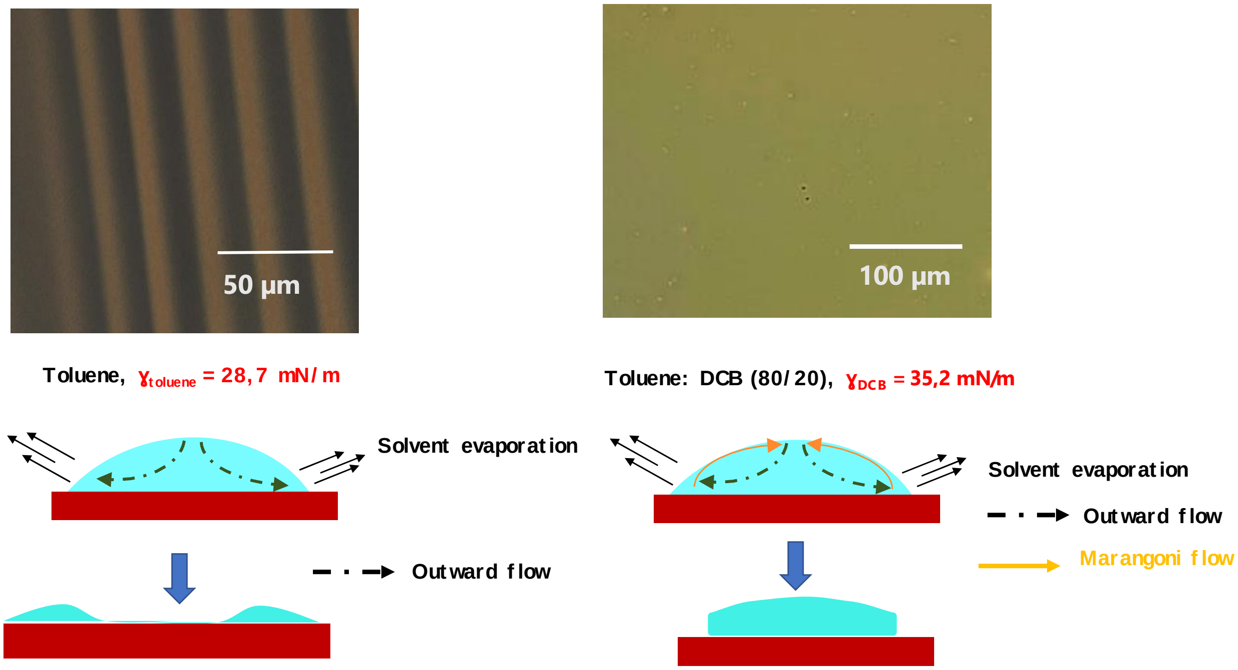

Figure 34. OM images of P3HT coated at 0.2 mm.s^{-1} at 65 °C on a glass substrate from toluene (left) and a blend of toluene and o-DCB, 80: 20 volume ratio (right). Schematic illustration of film and stripe formation via Marangoni flow.

b) Orientation and the aligned domains of P3HT

The basic idea here is to use a synergistic effect of the co-solvents to locally control the drying and the formation of a uniform film, as well as to enhance the crystallinity of the polymer. Thus, co-crystallizable solvents can play a double role, acting as nucleating agents for the crystallization of P3HT and, at the same time, contributing to the control of the solvent evaporation rate and the surface tension gradients (the Bénard-Marangoni instabilities) to create uniform, unpatterned and pinhole-less thin films. The nature of the solvent and co-solvent is an important parameter that can influence morphology and crystallinity. In fact, the interaction of solvent/co-colvent and solute affects the nucleation and growth kinetics. One effective way to control the morphology and crystallinity of conjugated polymers is the use of crystallizable solvents. In such way the crystallizable solvents can serve as solvent and nucleating agent for the conjugated polymers at temperatures above the solvents melting temperature. While the polymer is cooled below the melting point of the solvent, the crystallizable solvent becomes a substrate. Epitaxy usually occurs between a polymer and a crystalline substrate. On such crystalline substrate the conjugated polymers can be oriented. Similar synergistic effects between the Marangoni effect and nucleation agents have been reported for P3HT uniaxially aligned during deposition by directional epitaxial crystallization with 1,3,5-trichlorobenzene (TCB).[90] We have investigated the effect of two different co-crystallizable solvents, naphthalene (Naph) and TCB.

1) A study of P3HT: Naph

We investigated first the effect of Naph as crystallizable solvent on the structure and the morphology of P3HT. The concentration of Naph in toluene was varied from 1 to 10 mg.ml^{-1} and the temperature of the substrate was regulated between 30°C and 75 °C. The blading speeds ranged from 0.2 mm.s^{-1} to 0.7 mm.s^{-1}. The Naph was removed under vacuum at 50 °C ater film deposition. The first experiment was carried out using a solution containing 1 mg.ml^{-1} of Naph at substrate temperature of 90 °C. The typical morphology of obtained film is reported in Figure 35. According to the figure, a continuous and homogenous film with flat surface was produced. In comparison to the film prepared in the same conditions without adding the Naph, the stripe pattern was absent. This confirms that the Naph acts as co-solvent that changes the surface tension, resulting in a continuous film deposition via inverted Marangoni effect.

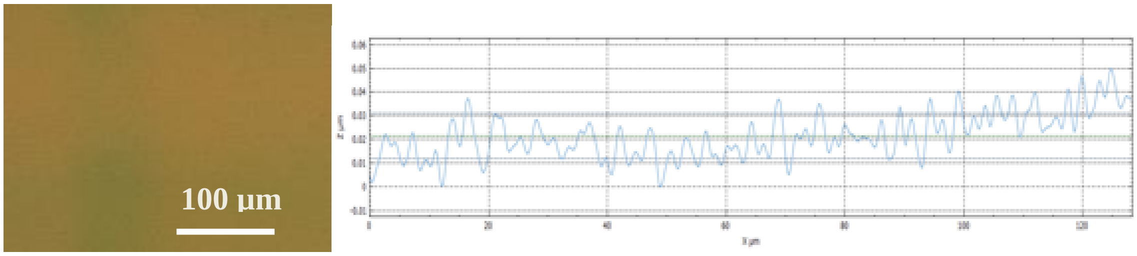

Figure 35. Optical image of P3HT film coated at the speed of 0.2 mm.s^{-1} and at 65 °C from a solution of 1 mg.ml^{-1} of naphthalene (left). Typical profile extracted from the image (right).

To gain further insight on the effect of the nucleating ability of Naph, we performed a systematic study of the influence of the temperature and the concentration of Naph. Three deposition temperatures, 30 °C, 50 °C and 70 °C, were studied while the concentration of Naph was increased to 10 mg.ml^{-1} and the blading speed was varied from 0.2 mm.s^{-1} to 1 mm.s^{-1}. After sublimation of Naph, flat surface of the P3HT film was obtained. The surface of the film was observed with OP and AFM. Topography images of thin films of P3HT with directionally aligned domains onto glass substrates are shown in Figure 36.

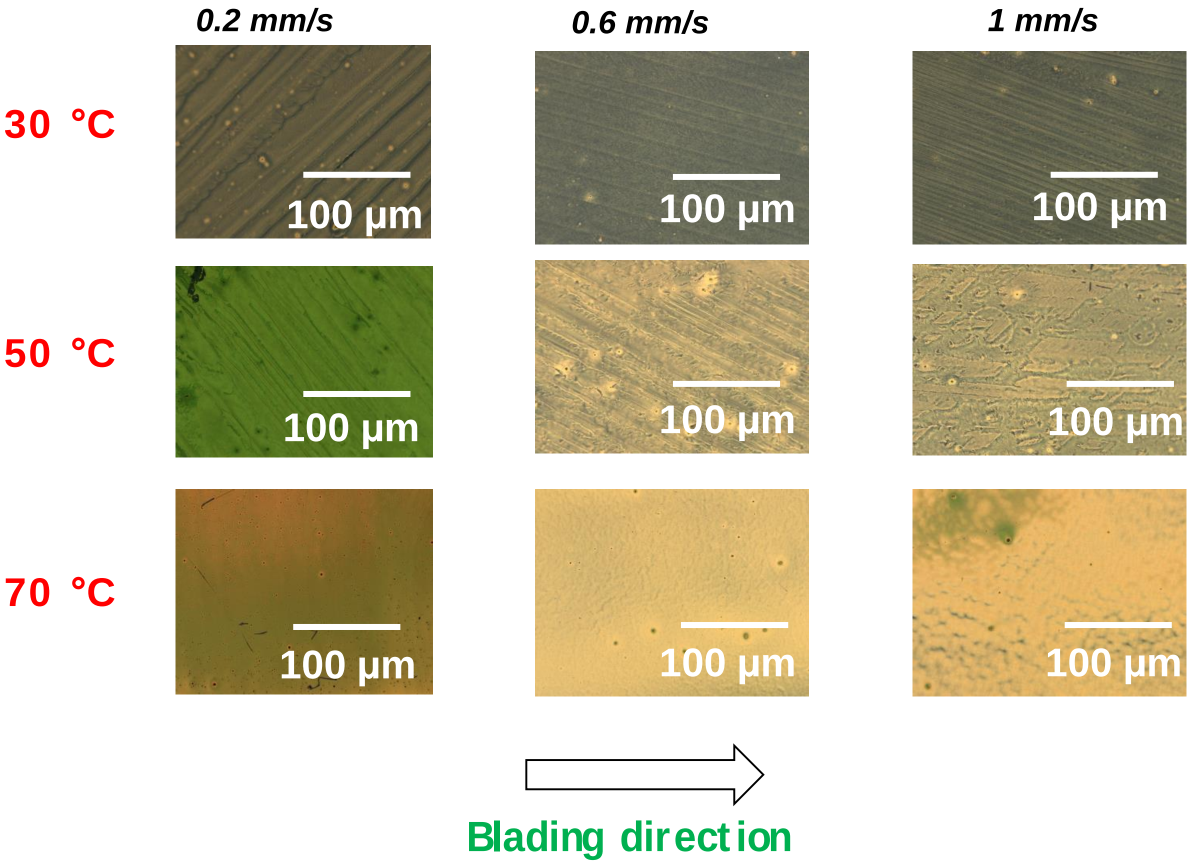

Figure 36. OM images of anisotropic crystalline films of P3HT obtained by epitaxial growth and crystal alignment after directional solidification on a crystallisable solvent. P3HT was coated at different speeds, 0.2 mm.s^{-1}, 0.6 mm.s^{-1}, 1 mm.s^{-1}, and at different temperatures on a glass substrate. Film coated from a solution of P3HT/Naph (10 mg/60 mg), 3 ml toluene.

Well-aligned domains over the large area are observed. The domains form aligned structure even on few-hundred-micrometer scale. Conversely, isotropic morphology was observed when the polymer was coated at 70 °C. It is clear from the images that the uniformly aligned domains appear with the increase of the nucleating agent content. When the temperature reaches 70 °C the domain orientation is lost and isotropic morphology appears. These results indicate that the nucleating agent and the deposition temperature are the key parameters in the ordered structure formation.

We identify two stages in the growth and domain orientation mechanism, related to the film drying: (I) slow solvent-evaporation resulting in aligned domains, (II) rapid solvent-evaporation resulting in misaligned domains. When the substrate is held at a temperature much lower than the boiling point of the toluene solvent (120°C), the film drying time is too long to allow the initiation of heterogeneous crystallization and uniform, continuous films with highly ordered domains are observed, as shown by OM images. In this case the crystalline domain orientation of the P3HT films depends on nucleation and crystal growth. Heterogeneous nucleation process in which the Naph acts as a nucleation site is the first step in the formation of polymer aggregates. The Naph crystals formed serve as substrate for the epitaxial growth of P3HT, leading to formation of highly oriented Naph-P3HT films with larger domains. Rapid solvent evaporation at high temperature (70°C) results in high nucleation rate of Naph with too many crystal seeds that favors ill-epitaxy growth with many sites of Naph leading to small and misaligned domains.

Birefringent films were obtained according to cross-polarized images, and a dichroic ratio R > 1.0 was observed indicating a preferential alignment of the domains with respect to the blading direction (curves not shown). The dichroic ratio R is defined as the maximum of the absorption of the polymer peak in the direction parallel to blading divided by that in the perpendicular direction. An increase of the substrate temperature causes a decrease in dichroism.

Raman measurements were recorded on two zones of the sample: in an aligned domain (zone A) and at the boundary of the aligned domain, in the area between aligned domains (zone B). For both zones the Raman spectra were recorded with the incident laser light polarized parallel and perpendicular to the alignment direction of the domain. The resulting spectra are shown in Figure 37. Morphological features of Naph-P3HT films show an apparent aggregate structure that is unidirectional and closely arranged. All the aggerates are composed of grains stacked in the blading direction (AFM images inset of Figure 37). The strongest signal was recorded when the alignment direction was parallel to incident laser polarization;

conversely, the weakest signal was observed when the alignment direction was perpendicular to it, indicating anisotropic orientation of P3HT chains perpendicular to the blading direction.

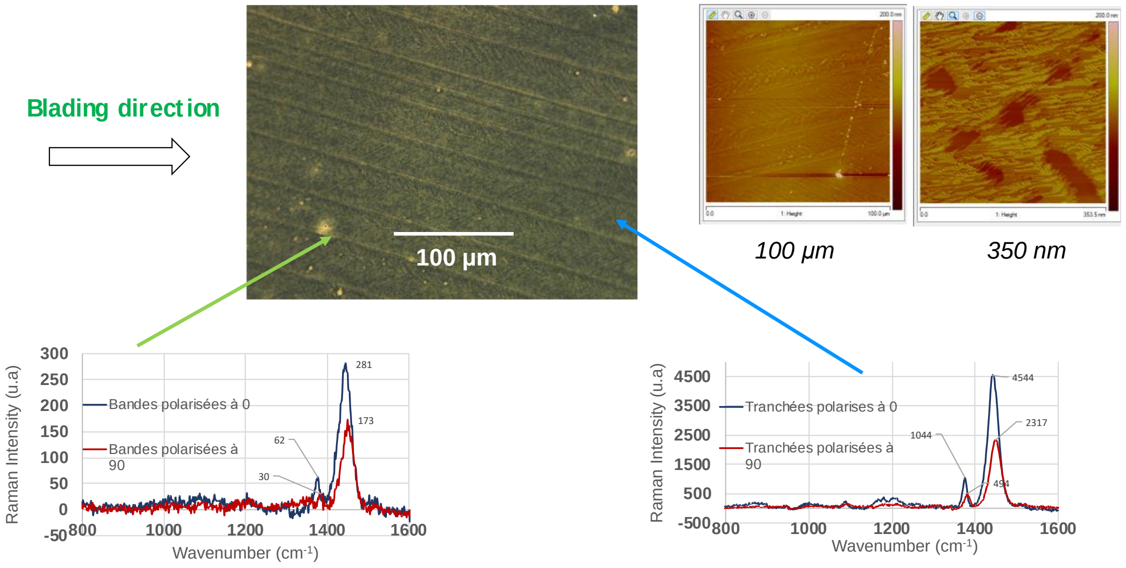

Figure 37. Comparison of polarized Raman spectra of P3HT film coated from a solution of P3HT/naphtalene (10 mg /60 mg), 3 ml toluene, with a speed of 0.2 mm.s^{-1}, at 30° C, (a) left misaligned domain (zone B), (b) right aligned domain (zone A). Top right AFM enlarged images showing grains stacked in the blading direction.

Thus, the increase of peak intensities in the parallel direction confirms that the polymer chains in zone A are aligned parallel to the blading direction. Table 1 summarizes the peak positions and full width at half maximum (FWHM) values of the C=C mode, the intensity of the C=C mode, and the peak shift of zone A with respect to zone B. The peak at ~1443 cm^{-1} is much narrower than that in the perpendicular direction. The FWHM are 34.5, 42.3 cm^{-1}, for zone A for parallel and perpendicular direction, and 39.2, 53.4 cm^{-1}, for zone B for parallel and perpendicular direction, respectively, indicating a higher degree of ordering in this zone in the parallel direction. Moreover, there is a 8 cm^{-1} shift to lower wavenumbers (lower energy), of the symmetric C═C stretching mode for the aligned domain (zone A) which is sensitive to π-electron delocalization along the backbone. A shift of only 4 cm^{-1} is observed for misaligned domain (zone

B). Such a shift of the Raman peak position towards lower energy, as well as an increase of the intensities of all peaks with the polarization of the beam have been reported and assigned to the polymer chain orientation in the direction of the polarization of the incident beam [91, 92]. Therefore, the remarkable increase in peak intensity, the narrower FWHM and the shift to a lower wavenumber indicate higher degree of the alignment. For the misaligned domain the trend is similar but with lower magnitude.

Table 1. Summary of the peak position and FWHM of the C=C mode, as well as the peak shift for zones A and B, at two laser polarizations (parallel and perpendicular to blading direction).

	Misaligned domain (zone B)	Aligned domain (zone A)
FWHM (cm^{-1}) Of the C=C	0 ° : 34. 5 90 ° : 42.3	0° : 39.2 90° : 53.4
Intensity (arb.u.)	0° : 281 90° : 173	0° : 4544 90° : 2261
Peak shift (cm^{-1})	0° : 1445.2 90° : 1449.2 Shift of 4 cm^{-1}	0° : 1440.5 90° : 1448 Shift of 8 cm^{-1}

These results are supported by the evolution of the polarized UV-Vis absorption spectra as functions of the temperature and the film deposition speed. For all samples the maximum absorption was observed when the incident polarization was perpendicular to the blading direction. The dichroic ratio decreased with film deposition temperature. The ratio was more significant at low deposition speeds.

2) Study on the effect of nucleating agent: 1, 3, 5 trichlorobenzene: P3HT

TCB is one of the crystallisable solvent that is commonly applied as a heterogeneous nucleating agent in order to induce molecular orientation of conjugated polymers. Thus, we decided to explore its capability to induce crystallisation and align domains. In the first experiment, we used the same conditions as those optimized for Naph, toluene as solvent: room temperature, and a 1:5 ratio of TCB to P3HT. The films were coated at different speeds ranging from 0.1 mm.s^{-1} to 4 mm.s^{-1}. Topographic analyses of surfaces were investigated using OM (not shown here). The films exhibit many of the features as those coated from solutions containing naphatalene. While no aligned growth of crystalline domains was observed on a large scale, the results were similar to those of naphthalene-film under ill conditions. So, changing the nucleating agent from naphthalene to TCB does not readily lead to the formation of oriented domains but rather needs optimization. Thus, by changing the processing conditions by increasing the TCB composition of blend from 10 mg to 100 mg, and by using dichlorobenzene, instead of toluene, as solvent, we succeeded in forming a uniaxially orientated P3HT film, as previously reported.[93, 94] The expected morphology of spherulite-like structure, as reported, was observed. The films were deposited on glass substrates at room temperature with blading speeds ranging from 0.1 mm.s^{-1} to 4 mm.s^{-1}, see Figure 38. At the blading speed of 0.4 mm.s^{-1} the texture observed corresponds to single spherulites. At higher deposition speeds (4 mm.s^{-1}) highly crystalline unidirectional fibrous structures exhibiting a dichroic ratio R larger than one are formed.

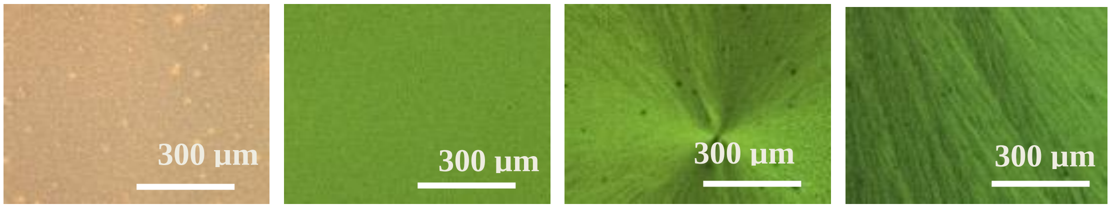

Figure 38. OM images of P3HT coated from a solution of DCB and TCB (100 mg) at the speeds of 0.4 mm.s^{-1}, 0.6 mm.s^{-1}, 1 mm.s^{-1} and 4 mm.s^{-1} at 30 °C on a glass substrate.

3) Study on the effect of the nature of conjugated polymers: block copolymer (P3HT-*b*-PT)

To extend this approach to other semi-crystalline conjugated polymers, we explored the impact of the conjugated backbone on domain alignment under shear. We chose a block copolymer, poly-(3-hexylthiophene)-*b*-poly(thiophene)-*b* P3HT-*b*-PT, having P3HT as the first rod block and polyhiophene as the second rod block. These block copolymers have strong ability to assembly into ordered domains. Previous study has shown that P3HT-*b*-PT copolymers exhibit microphase-separated morphology and display competitive crystallinity, with one block or the other dominating the crystalline and morphology. The morphologies and crystallites observed are determined by the ratio of block sizes [95]. We investigated whether Naph had a greater nucleating effect upon a block copolymer, Figure 39. The film deposition conditions were similar to those of the previous experiments on P3HT/Naph: 10 mg of copolymer in 1 ml of toluene, the copolymer-to-Naph mass ratio was 1: 6, the deposition temperature was 30° C, the blade speeds were varied between 0.2 mm.s^{-1} and 1 mm.s^{-1}. Topographic analyses of surfaces by OM shown in Figure 38 reveal the presence of small crystallites in the form of dendrites. We did not observe a fully structured film formation as observed previously with P3HT. We noticed also a decrease in the size of the dendrites with increasing the blading speed.

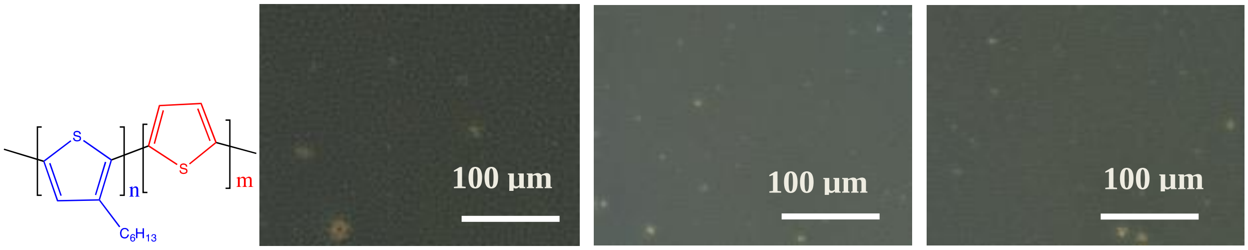

Figure 39. Chemical structure of block copolymer (P3HT-b-PT), OM images of the (P3HT-b-PT) film coated on a glass substrate at the blade speed of 0.2 mm.s^{-1} (left), 0.4 mm.s^{-1} (center) and 1 mm.s^{-1} (right).

To deepen this morphological study, we investigated the organization of the observed dendrites by AFM. The images obtained allow us to observe a shish-kebab superstructure shown in Figure 40. Within this structure ribbons, or rather large fibres constitute the shish on which the nano-fibrils stack perpendicularly to form the kebab. Shish-kebab morphologies were observed during epitaxial crystallization of P3HT in the presence of TCB and pyridine, by Brinkmann and coworkers [96]. In such morphology, a shish fiber, P3AT chains were oriented parallel to the long axis of TCB needles that were preferably formed in pyridine. In a kebab fibril, folded P3AT chains packed with the π-stacking direction parallel to the fibril axis.

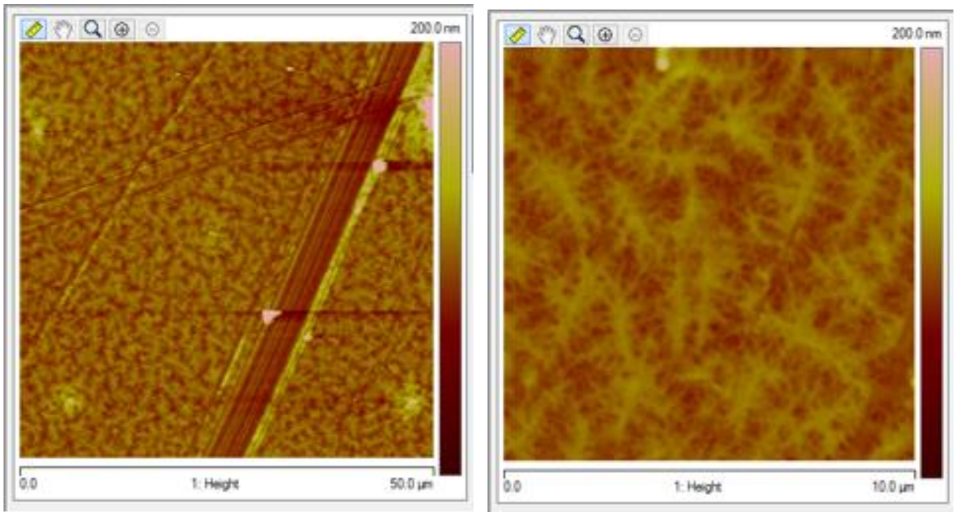

Figure 40. AFM images of the block copolymer (P3HT-b-PT) coated on a glass substrate from 10 mg.ml^{-1} of solution of copolymer with naphthalene, 1:6 of mass ratio, at 30 °C at the blading speed of 0.2 mm.s^{-1}. The images show the shish-kebab morphology induced by directional coating.

Conclusion

In this review, we have discussed the major advances that have recently been achieved in the emerging field of meniscus-guided printing of OSC materials, with particular emphasis on materials and physical chemistry of surface thin films that have the potential to achieve improved electrical performance devices. We began with brief an overview of the recent advances in MGC techniques. Then we focused on large-scale fabrication of highly regular deposits, stripes and ribbons, produced by MGC methods. A crucial step for further integration of OSC based devices into real applications is crystal alignment and patterning. Crystal alignment can be achieved by MGC methods where receding of meniscus is controlled. OSC patterning relies on selective nucleation and spatial confinement of the crystallization in evaporative regime. In this regime, stick-slip phenomenon is observed, resulting to formation of regular line patterns of the OSC molecules perpendicular to the coating direction. Moreover, during the coating process the triple contact line is not kept pinned, resulting in a stick-slip motion, repeated pinning and depinning. The OSC molecules transport to the edge during pinning of the triple contact line, i.e. stick, thus forming a deposit. Then, the triple contact line jumps, (i.e. slip) to a new position and a deposit is then formed. These pinning and depinning events alternate as solvent evaporates and, ultimately, lead to the formation of periodic deposit, which is governed by a competition between the capillary force and the pinning force. The width and interval of the patterns can be manipulated by varying the OSC concentration, speed and surface energy of the substrate. Through a selection of significant examples from the recent literature, we have systematically analysed the effect of several experimental parameters, the OSC concentration, coating speed, solvent evaporation, surface tension of solvents, and nature of substrates, on pattern formation. We have seen that solute transport during solution coating is very sensitive to surface tension gradient, caused by temperature or concentration differences. The blade speed, and the evaporation rate of the solvent have been identified as the main control parameters. In the last section we have investigated the spontaneous pattern formation by blade coating of a P3HT solution on homogeneous surfaces. The height, width and periodicity of the patterns were controlled by adjusting the process parameters: blade speed, surface tension of the solvent, and surface energy of the substrate. The pattern formation is due to the Bénard-Marangoni convection. Adjusting the gradient of surface tension with co-solvents having high surface tension and high boiling point, suppresses the Marangoni effect, and promotes highly homogeneous thin film deposition. On the other hand, the addition of crystallizable co-solvent results in large-area aligned domains of P3HT, attributable to synergistic effects of crystallisable solvents and shearing forces. We investigated the growth mechanism of aligned domains of P3HT during the blade coating and found that the correct choice of co-solvents and appropriate solvent ratio are in favor of aligned P3HT domain growth. This finding provides a simple and generally applicable method to fabricate lithography-free patterning of conjugated polymer arrays for various applications. Understanding the facil patterning of OSC via MGC methods can provide insights on printed organic electronics and flexible devices.

Experimental section

Regioregular poly(3-hexylthiophene-2,5-diyl) with purity > 90% and molecular weight in the range of 50-100 kDa was purchased from Aldrich and used without any purification. Block copolymer (P3HT-b PT) was synthesized following the procedure reported by Lee *et al.* [95]. P3HT and copolymer solutions were prepared at different concentrations in toluene or 1,2-dichlorobenzene. The solutions were stirred at 50 °C overnight to totally dissolve the polymer. For thin-film deposition, we used an Erichsen Doctor Blade system operated under air with a blade distance from the substrate of 50 μm. The substrates (2×2 cm^2 glass slide, silicon wafer, Al_2O_3 ALD) were cleaned prior to use by sonicating in acetone and isopropanol for 15 minutes and then dried with dry N_2. Moreover, 15 minutes of ozone treatment were applied in order to remove organic residues on the substrate surface. The 10 μl of polymer solution was injected into the gap between the deposition blade and the substrate. Then, the substrate was pulled out at an appropriate deposition speed in the range of 0.1 - 5.0 $mm.s^{-1}$. The temperature of the substrate during blading was fixed at the appropriate temperature. After blading, the film was left drying for 15 min. The film samples formed by epitaxial growth on removable solvents were fabricated by blading polymers on a glass or a SiO_2/Si substrate, followed by drying at 50 °C in vacuum. The solvents used were toluene or 1,2-dichlorobenzene in the presence of various concentrations of 1,3,5-trichlorobenzene or naphthalene. The film thickness was measured with a Veeco DEKTAK 150 Profilometer, with a 1.5 μm radius stylus tip, and a 5 mg stylus force. The surface morphology of polymer films was characterized by atomic force microscopy in non-contact mode (Seiko Instruments SPI3800N equipped with SPA400). The atomic force microscopy (AFM) experiments were performed on thin films on freshly prepared substrates. Multimode 8 and Nanoscope V controller (Veeco Instrument) were used for AFM imaging. AFM images were obtained in tapping mode using non-contact mode tips from Nanoworld (Pointprobe® tip, NCHR type) with the spring constant of 42 $N.m^{-1}$ and tip radius smaller than 8 nm. Optical microscope images were taken with a 3D microscope (Leica DCM8 from Leica Microsystems, Heerbrugg, Switzerland). Polarized transmission spectra were measured on a 6800 UV/Vis JENWAY spectrophotometer and air was defined as the baseline for all measurements. The polarized spectra of the P3HT films on the glass substrates were recorded with the light beam polarized using a Melles griot polarizer. The spectra were obtained at 0°, 45° and 90° incidence in the transmission mode with s polarization both parallel and perpendicular to the balding direction by rotating the polarizer. The reference spectrum with each polarization of the glass substrate was subtracted from each sample spectrum. Raman spectroscopy measurements have been carried out with a LabRAM HR800 micro spectrometer (Horiba Scientific) equipped with a solid state laser emitting at 532 nm. The incident beam was focused on the sample surface using a 100X magnification lens (numerical aperture of

0.9). The Raman signal was collected through the same objective in a backscattering configuration and acquired by a CCD detector (Synapse Horiba Scientific). Intensity Spectra were acquired at a laser power of 30 mW with 6 s exposure time and 20 accumulations each.

References

1. Glotzer, S.C. and M.J. Solomon, *Anisotropy of building blocks and their assembly into complex structures.* Nature Materials, 2007. **6**: p. 557.
2. Kimura, T., *Evaporation-induced Self-assembly Process Controlled for Obtaining Highly Ordered Mesoporous Materials with Demanded Morphologies.* The Chemical Record, 2016. **16**(1): p. 445-457.
3. Ozin, G.A., et al., *Nanofabrication by self-assembly.* Materials Today, 2009. **12**(5): p. 12-23.
4. Park, W.K., et al., *Large-scale patterning by the roll-based evaporation-induced self-assembly.* Journal of Materials Chemistry, 2012. **22**(43): p. 22844-22847.
5. W., P., et al., *A Zone-Casting Technique for Device Fabrication of Field-Effect Transistors Based on Discotic Hexa-peri-hexabenzocoronene.* Advanced Materials, 2005. **17**(6): p. 684-689.
6. Jaeyoung, J., et al., *Highly Crystalline Soluble Acene Crystal Arrays for Organic Transistors: Mechanism of Crystal Growth During Dip-Coating.* Advanced Functional Materials, 2012. **22**(5): p. 1005-1014.
7. Giri, G., et al., *Tuning charge transport in solution-sheared organic semiconductors using lattice strain.* Nature, 2011. **480**: p. 504.
8. Diao, Y., et al., *Solution coating of large-area organic semiconductor thin films with aligned single-crystalline domains.* Nature Materials, 2013. **12**: p. 665.
9. Mennig, M. and M. Aegerter, *Handbook on Sol-Gel Technologies for Glass Producers and Users*. 2004.
10. Fukuda, K. and T. Someya, *Recent Progress in the Development of Printed Thin-Film Transistors and Circuits with High-Resolution Printing Technology.* Advanced Materials, 2017. **29**(25): p. 1602736.
11. Mai, Y. and A. Eisenberg, *Self-assembly of block copolymers.* Chemical Society Reviews, 2012. **41**(18): p. 5969-5985.
12. Diao, Y., et al., *Morphology control strategies for solution-processed organic semiconductor thin films.* Energy & Environmental Science, 2014. **7**(7): p. 2145-2159.
13. Le Berre, M., Y. Chen, and D. Baigl, *From Convective Assembly to Landau−Levich Deposition of Multilayered Phospholipid Films of Controlled Thickness.* Langmuir, 2009. **25**(5): p. 2554-2557.
14. Ghosh, M., F. Fan, and K.J. Stebe, *Spontaneous Pattern Formation by Dip Coating of Colloidal Suspensions on Homogeneous Surfaces.* Langmuir, 2007. **23**(4): p. 2180-2183.
15. Wedershoven, H.M.J.M., J.C.H. Zeegers, and A.A. Darhuber, *Polymer film deposition from a receding solution meniscus: The effect of laminar forced air convection.* Chemical Engineering Science, 2018. **181**: p. 92-100.
16. Gu, X., et al., *The meniscus-guided deposition of semiconducting polymers.* Nature Communications, 2018. **9**(1): p. 534.
17. Sun, H., et al., *Unidirectional coating technology for organic field-effect transistors: materials and methods.* Semiconductor Science and Technology, 2015. **30**(5): p. 054001.
18. Patel, B.B. and Y. Diao, *Multiscale assembly of solution-processed organic electronics: the critical roles of confinement, fluid flow, and interfaces.* Nanotechnology, 2017. **29**(4): p. 044004.
19. Khim, D., et al., *Uniaxial Alignment of Conjugated Polymer Films for High-Performance Organic Field-Effect Transistors.* Advanced Materials, 2018. **30**(20): p. 1705463.

20. Qu, G., J.J. Kwok, and Y. Diao, *Flow-Directed Crystallization for Printed Electronics.* Accounts of Chemical Research, 2016. **49**(12): p. 2756-2764.
21. Peng, B., et al., *Solution-Processed Monolayer Organic Crystals for High-Performance Field-Effect Transistors and Ultrasensitive Gas Sensors.* Advanced Functional Materials, 2017. **27**(29): p. 1700999.
22. Wang, C., et al., *Organic semiconductor crystals.* Chemical Society Reviews, 2018. **47**(2): p. 422-500.
23. Jiang, L., et al., *Millimeter-Sized Molecular Monolayer Two-Dimensional Crystals.* Advanced Materials, 2011. **23**(18): p. 2059-2063.
24. Shan, L., et al., *Monolayer Field-Effect Transistors of Nonplanar Organic Semiconductors with Brickwork Arrangement.* Advanced Materials, 2015. **27**(22): p. 3418-3423.
25. Marszalek, T., et al., *Transparent and air stable organic field effect transistors with ordered layers of dibenzo[d,d]thieno[3,2-b;4,5-b']dithiophene obtained from solution.* Optical Materials, 2012. **34**(10): p. 1660-1663.
26. Yamamura, A., et al., *Wafer-scale, layer-controlled organic single crystals for high-speed circuit operation.* Science Advances, 2018. **4**(2): p. eaao5758.
27. Hamai, T., et al., *Tunneling and Origin of Large Access Resistance in Layered-Crystal Organic Transistors.* Physical Review Applied, 2017. **8**(5): p. 054011.
28. Arai, S., et al., *Semiconductive Single Molecular Bilayers Realized Using Geometrical Frustration.* Advanced Materials, 2018. **30**(23): p. 1707256.
29. Santos, M.T., et al., *Changes in the solid-liquid interface during the growth of Bi12SiO20, Bi12GeO20 and LiNbO3 crystals grown by the Czochralski method*. Vol. 156. 1995. 413–420.
30. Zhou, Z., et al., *Inch-Scale Grain Boundary Free Organic Crystals Developed by Nucleation Seed-Controlled Shearing Method*. Vol. 10. 2018.
31. Peng, B., Z. Wang, and P.K.L. Chan, *A simulation-assisted solution-processing method for a large-area, high-performance C10-DNTT organic semiconductor crystal.* Journal of Materials Chemistry C, 2016. **4**(37): p. 8628-8633.
32. Janneck, R., et al., *Predictive Model for the Meniscus-Guided Coating of High-Quality Organic Single-Crystalline Thin Films.* Advanced Materials, 2016. **28**(36): p. 8007-8013.
33. Birnie, D.P., *Rational solvent selection strategies to combat striation formation during spin coating of thin films.* Journal of Materials Research, 2011. **16**(4): p. 1145-1154.
34. Birnie, D.P., *A Model for Drying Control Cosolvent Selection for Spin-Coating Uniformity: The Thin Film Limit.* Langmuir, 2013. **29**(29): p. 9072-9078.
35. Zhang, Z., et al., *Marangoni-Effect-Assisted Bar-Coating Method for High-Quality Organic Crystals with Compressive and Tensile Strains.* Advanced Functional Materials, 2017. **27**(37): p. 1703443.
36. Wang, Z., et al., *Marangoni Effect-Controlled Growth of Oriented Film for High Performance C8-BTBT Transistors.* Advanced Materials Interfaces, 2019. **6**(8): p. 1801736.
37. Jiang, Y., et al., *Fast Deposition of Aligning Edge-On Polymers for High-Mobility Ambipolar Transistors.* Advanced Materials, 2019. **31**(2): p. 1805761.
38. Giri, G., et al., *One-dimensional self-confinement promotes polymorph selection in large-area organic semiconductor thin films.* Nature Communications, 2014. **5**: p. 3573.
39. Diao, Y., et al., *Understanding Polymorphism in Organic Semiconductor Thin Films through Nanoconfinement.* Journal of the American Chemical Society, 2014. **136**(49): p. 17046-17057.
40. Galindo, S., et al., *Control of Polymorphism and Morphology in Solution Sheared Organic Field-Effect Transistors.* Advanced Functional Materials, 2017. **27**(25): p. 1700526.
41. Temiño, I., et al., *A Rapid, Low-Cost, and Scalable Technique for Printing State-of-the-Art Organic Field-Effect Transistors.* Advanced Materials Technologies, 2016. **1**(5): p. 1600090.
42. Kim, K., et al., *Facile and Microcontrolled Blade Coating of Organic Semiconductor Blends for Uniaxial Crystal Alignment and Reliable Flexible Organic Field-Effect Transistors.* ACS Applied Materials & Interfaces, 2019. **11**(14): p. 13481-13490.

43. Zhang, F., et al., *Solution-Processed Nanoporous Organic Semiconductor Thin Films: Toward Health and Environmental Monitoring of Volatile Markers.* Advanced Functional Materials, 2017. **27**(23): p. 1701117.
44. Zhang, F., et al., *Large Modulation of Charge Carrier Mobility in Doped Nanoporous Organic Transistors.* Advanced Materials, 2017. **29**(27): p. 1700411.
45. Niazi, M.R., et al., *Solution-printed organic semiconductor blends exhibiting transport properties on par with single crystals.* Nature Communications, 2015. **6**: p. 8598.
46. Ge, F., et al., *Bar-Coated Ultrathin Semiconductors from Polymer Blend for One-Step Organic Field-Effect Transistors.* ACS Applied Materials & Interfaces, 2018. **10**(25): p. 21510-21517.
47. Qu, G., et al., *Understanding Interfacial Alignment in Solution Coated Conjugated Polymer Thin Films.* Acs Applied Materials & Interfaces, 2017. **9**(33): p. 27863-27874.
48. Shaw, L., et al., *Microstructural Evolution of the Thin Films of a Donor–Acceptor Semiconducting Polymer Deposited by Meniscus-Guided Coating.* Macromolecules, 2018. **51**(11): p. 4325-4340.
49. Trefz, D., et al., *Tuning Orientational Order of Highly Aggregating P(NDI2OD-T2) by Solvent Vapor Annealing and Blade Coating.* Macromolecules, 2019. **52**(1): p. 43-54.
50. Wang, G., et al., *Aggregation control in natural brush-printed conjugated polymer films and implications for enhancing charge transport.* Proceedings of the National Academy of Sciences, 2017. **114**(47): p. E10066-E10073.
51. Persson, N.E., et al., *In situ Observation of Alignment Templating by Seed Crystals in Highly Anisotropic Polymer Transistors.* Chemistry of Materials, 2019.
52. Molina-Lopez, F., et al., *Enhancing Molecular Alignment and Charge Transport of Solution-Sheared Semiconducting Polymer Films by the Electrical-Blade Effect.* Advanced Electronic Materials, 2018. **4**(7): p. 1800110.
53. Haase, K., et al., *Solution Shearing of a High-Capacitance Polymer Dielectric for Low-Voltage Organic Transistors.* Advanced Electronic Materials. **0**(0): p. 1900067.
54. Wilczek, M., et al., *Modelling Pattern Formation in Dip-Coating Experiments.* Math. Model. Nat. Phenom., 2015. **10**(4): p. 44-60.
55. Doumenc, F. and B. Guerrier, *Self-patterning induced by a solutal Marangoni effect in a receding drying meniscus.* EPL (Europhysics Letters), 2013. **103**(1): p. 14001.
56. Doumenc, F., J.-B. Salmon, and B. Guerrier, *Modeling Flow Coating of Colloidal Dispersions in the Evaporative Regime: Prediction of Deposit Thickness.* Langmuir, 2016. **32**(51): p. 13657-13668.
57. Masuda, Y., et al., *Self-Assembly Patterning of Colloidal Crystals Constructed from Opal Structure or NaCl Structure.* Langmuir, 2004. **20**(13): p. 5588-5592.
58. Watanabe, S., et al., *Mechanism for Stripe Pattern Formation on Hydrophilic Surfaces by Using Convective Self-Assembly.* Langmuir, 2009. **25**(13): p. 7287-7295.
59. Yabu, H. and M. Shimomura, *Preparation of Self-Organized Mesoscale Polymer Patterns on a Solid Substrate: Continuous Pattern Formation from a Receding Meniscus.* Advanced Functional Materials, 2005. **15**(4): p. 575-581.
60. Kim, H.S., et al., *Nanoparticle Stripes, Grids, and Ribbons Produced by Flow Coating.* Advanced Materials, 2010. **22**(41): p. 4600-4604.
61. Park, S., et al., *Large-Area Assembly of Densely Aligned Single-Walled Carbon Nanotubes Using Solution Shearing and Their Application to Field-Effect Transistors.* Advanced Materials, 2015. **27**(16): p. 2656-2662.
62. Li, Y., et al., *Patterning technology for solution-processed organic crystal field-effect transistors.* Science and Technology of Advanced Materials, 2014. **15**(2): p. 024203.
63. Zhang, C., et al., *Facile One-Step Growth and Patterning of Aligned Squaraine Nanowires via Evaporation-Induced Self-Assembly.* Advanced Materials, 2008. **20**(9): p. 1716-1720.

64. Li, L., et al., *Growth of Ultrathin Organic Semiconductor Microstripes with Thickness Control in the Monolayer Precision.* Angewandte Chemie International Edition, 2013. **52**(48): p. 12530-12535.
65. Wu, K., et al., *Controlled Growth of Ultrathin Film of Organic Semiconductors by Balancing the Competitive Processes in Dip-Coating for Organic Transistors.* Langmuir, 2016. **32**(25): p. 6246-6254.
66. Wang, B., et al., *Fast patterning of oriented organic microstripes for field-effect ammonia gas sensors.* Nanoscale, 2016. **8**(7): p. 3954-3961.
67. Liu, N., et al., *In Situ Growing and Patterning of Aligned Organic Nanowire Arrays via Dip Coating.* Langmuir, 2009. **25**(2): p. 665-671.
68. Jang, J., et al., *Highly Crystalline Soluble Acene Crystal Arrays for Organic Transistors: Mechanism of Crystal Growth During Dip-Coating.* Advanced Functional Materials, 2012. **22**(5): p. 1005-1014.
69. Nam, S., et al., *High-Performance Triethylsilylethynyl Anthradithiophene Transistors Prepared without Solvent Vapor Annealing: The Effects of Self-Assembly during Dip-Coating.* ACS Applied Materials & Interfaces, 2013. **5**(6): p. 2146-2154.
70. Park, S., et al., *Large-area formation of self-aligned crystalline domains of organic semiconductors on transistor channels using CONNECT.* Proceedings of the National Academy of Sciences, 2015. **112**(18): p. 5561-5566.
71. Giri, G., et al., *High-Mobility, Aligned Crystalline Domains of TIPS-Pentacene with Metastable Polymorphs Through Lateral Confinement of Crystal Growth.* Advanced Materials, 2014. **26**(3): p. 487-493.
72. Janneck, R., et al., *Influence of the Surface Treatment on the Solution Coating of Single-Crystalline Organic Thin-Films.* Advanced Materials Interfaces, 2018. **5**(12): p. 1800147.
73. Zhao, H., et al., *Fabrication of highly oriented large-scale TIPS pentacene crystals and transistors by the Marangoni effect-controlled growth method.* Physical Chemistry Chemical Physics, 2015. **17**(9): p. 6274-6279.
74. Rogowski, R.Z., et al., *Solution Processing of Semiconducting Organic Molecules for Tailored Charge Transport Properties.* The Journal of Physical Chemistry C, 2011. **115**(23): p. 11758-11762.
75. Zhang, K., et al., *Crystallization Control of Organic Semiconductors during Meniscus-Guided Coating by Blending with Polymer Binder.* Advanced Functional Materials, 2018. **28**(50): p. 1805594.
76. Jiang, Y., Y. Guo, and Y. Liu, *Engineering of Amorphous Polymeric Insulators for Organic Field-Effect Transistors.* Advanced Electronic Materials, 2017. **3**(11): p. 1700157.
77. Ji, D., et al., *Surface Polarity and Self-Structured Nanogrooves Collaboratively Oriented Molecular Packing for High Crystallinity toward Efficient Charge Transport.* Journal of the American Chemical Society, 2017. **139**(7): p. 2734-2740.
78. Zhao, W., et al., *A Facile Method for the Growth of Organic Semiconductor Single Crystal Arrays on Polymer Dielectric toward Flexible Field-Effect Transistors.* Advanced Functional Materials. **0**(0): p. 1902494.
79. Chai, Z., S.A. Abbasi, and A.A. Busnaina, *Scalable Directed Assembly of Highly Crystalline 2,7-Dioctyl[1]benzothieno[3,2-b][1]benzothiophene (C8-BTBT) Films.* ACS Applied Materials & Interfaces, 2018. **10**(21): p. 18123-18130.
80. Qu, G., et al., *Understanding Film-To-Stripe Transition of Conjugated Polymers Driven by Meniscus Instability.* ACS Applied Materials & Interfaces, 2018. **10**(47): p. 40692-40701.
81. Kim, J.-O., et al., *Inorganic Polymer Micropillar-Based Solution Shearing of Large-Area Organic Semiconductor Thin Films with Pillar-Size-Dependent Crystal Size.* Advanced Materials, 2018. **30**(29): p. 1800647.
82. Janneck, R., et al., *Highly Crystalline C8-BTBT Thin-Film Transistors by Lateral Homo-Epitaxial Growth on Printed Templates.* Advanced Materials, 2017. **29**(44): p. 1703864.

83. Peters, K., et al., *Formation of blade and slot die coated small molecule multilayers for OLED applications studied theoretically and by XPS depth profiling.* AIP Advances, 2016. **6**(6): p. 065108.
84. Abbel, R., et al., *Toward high volume solution based roll-to-roll processing of OLEDs.* Journal of Materials Research, 2017. **32**(12): p. 2219-2229.
85. Liang, J., et al., *Elastomeric polymer light-emitting devices and displays.* Nature Photonics, 2013. **7**: p. 817.
86. Guo, F., et al., *The fabrication of color-tunable organic light-emitting diode displays via solution processing.* Light: Science &Amp; Applications, 2017. **6**: p. e17094.
87. Gieun, K., et al., *Roll-to-Roll Fabrication of PEDOT:PSS Stripes Using Slot-Die Head With μ-Tips for AMOLEDs*. Vol. PP. 2018. 1-9.
88. Smith, B.H., et al., *Controlling Polymorphism in Poly(3-Hexylthiophene) through Addition of Ferrocene for Enhanced Charge Mobilities in Thin-Film Transistors.* Advanced Functional Materials, 2015. **25**(4): p. 542-551.
89. Baibarac, M., et al., *SERS spectra of poly(3-hexylthiophene) in oxidized and unoxidized states.* Journal of Raman Spectroscopy, 1998. **29**(9): p. 825-832.
90. Dörling, B., et al., *Uniaxial macroscopic alignment of conjugated polymer systems by directional crystallization during blade coating.* Journal of Materials Chemistry C, 2014. **2**(17): p. 3303-3310.
91. Qu, S., et al., *Highly anisotropic P3HT films with enhanced thermoelectric performance via organic small molecule epitaxy.* Npg Asia Materials, 2016. **8**: p. e292.
92. Wood, S., J.R. Hollis, and J.-S. Kim, *Raman spectroscopy as an advanced structural nanoprobe for conjugated molecular semiconductors.* Journal of Physics D: Applied Physics, 2017. **50**(7): p. 073001.
93. Shaw, L., et al., *Direct Uniaxial Alignment of a Donor–Acceptor Semiconducting Polymer Using Single-Step Solution Shearing.* ACS Applied Materials & Interfaces, 2016. **8**(14): p. 9285-9296.
94. Chu, P.-H., et al., *Toward Precision Control of Nanofiber Orientation in Conjugated Polymer Thin Films: Impact on Charge Transport.* Chemistry of Materials, 2016. **28**(24): p. 9099-9109.
95. Lee, I.-H. and T.-L. Choi, *Importance of choosing the right polymerization method for in situ preparation of semiconducting nanoparticles from the P3HT block copolymer.* Polymer Chemistry, 2016. **7**(46): p. 7135-7141.
96. Brinkmann, M., et al., *Epitaxial Growth of Highly Oriented Fibers of Semiconducting Polymers with a Shish-Kebab-Like Superstructure.* Advanced Functional Materials, 2009. **19**(17): p. 2759-2766.

Author Contributions

The manuscript was written through contributions of all authors. All authors have given approval to the final version of the manuscript.

ACKNOWLEDGMENT

This work is supported by the French National Agency (ANR) in the frame of its program in defi tous les savoir (GATE project ANR-16-CE07-0024). M.R. gratefully recognizes LabEx CHARMMMAT for her internship funding. The authors thank, Platine platform facilities for confocal characterization, and A. F. gratefully recognizes funding within the ANR-16-CE09-0029-03 TIPTOP_1 project.

ABBREVIATIONS

AFM, Atomic force microscopy

ALD, atomic layer deposition

DBC, Doctor blade coating

EISA, evaporative induced self-assembly

MGC, meniscus guided coating

Naph, naphthalene

o-DCB, ortho dichlorobenzene

OM, optical microscopy

OFET, organic field-effect transistor

OLED, organic light emeting diode

OSC, organic semiconductor

OSSC, organic semiconductor single crystal

P3HT, poly(3-hexylthiophene-2,5-diyl)

PMMAA, poly(methyl methacrylate)

SEM, scanning electron microscopy

TEM, transmission electron microscopy

TIPS-PEN, TIPS-pentacene

TCB, 1,3,5-trichlorobenzene

Chemical structures for selected organic semiconductor abbreviations

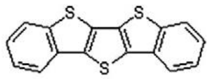

dibenzo[d,d]thieno [3,2-b;4,5-b’] dithiophene, DBTDT

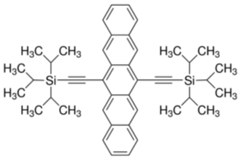

6,13-bis(triisopropylsilylethynyl)pentacene, TIPS-PEN

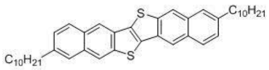

2,9 didecyldinaphtho[2,3-b:2′,3′-f]thieno[3,2-b]thiophene, C10-DNTT

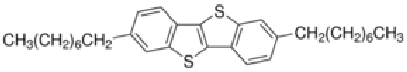

2,7-dioctyl[1]benzothieno[3,2-b][1]benzothiophene, C8-BTBT

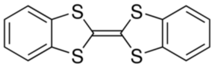

Dibenzo-tetrathiafulvalene, dibenzo-TTF, DB-TTF

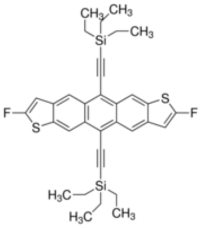

2,8-Difluoro-5,11-bis(triethylsilylethynyl)anthradithiophene, diF-TES-ADT

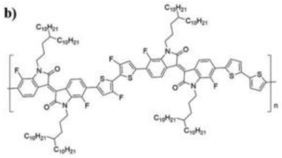

Poly(fluoroisoindigo-difluorobithiophene-fluoroisoindigo-bithiophene), PFIBI-BT

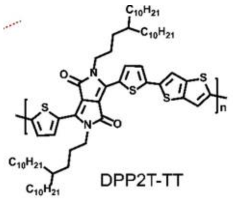

Poly(diketopyrrolopyrrole-thiophene-thieno[3,2,b]thiophene-thiophene), DPP2T-TT

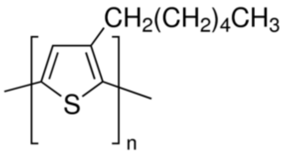

poly(3-hexylthiophene-2,5-diyl), P3HT

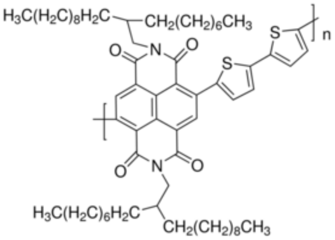

Poly{[*N*,*N*′-bis(2-octyldodecyl)-naphthalene-1,4,5,8-bis(dicarboxiimide)-2,6-diyl]-*alt*-5,5′-(2,2′-bithiophene)}, P(NDI2OD-T2)

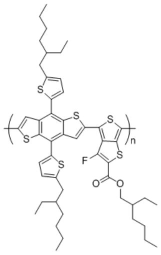

Poly[4,8-bis(5-(2-ethylhexyl)thiophen-2-yl)benzo[1,2-b;4,5-b’]dithiophene-2,6-diyl-alt-(4-(2-ethylhexyl)-3-fluorothieno[3,4-b]thiophene-)-2-carboxylate-2-6-diyl)], PBDTT-FTTE

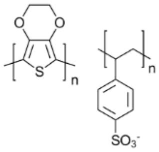

Poly(3,4-ethylenedioxythiophene)-poly(styrenesulfonate), PEDOT:PSS